AKNOWLEDGEMENTS

I would like to thank warmly all those who helped me so much during this year of work. In particular my supervisor Emanuela Barzi (Il Capo), who guided me enthusiastically day after day and revised my thesis manuscript with extreme care, Alexander Zlobin (Sasha) who enlightened me in solving the most critical problems, Joe Ozelis who explained me how to handle electronics, and Thomas Wokas who taught me how to work in a cryogenics laboratory.

I also want to thank all my young and senior CDF friends across Batavia Road. Their support and the great time spent together have been essential in making my year in the U.S. a productive and wonderful time.

Finally, many thanks to Peter Limon, Giovanni Pauletta, and John Tompkins who gave me the unique opportunity to come and do research in such a great laboratory as Fermilab.

INDEX

FOREWORD

In this thesis, the results of a research and development program performed at the Technical Division (TD) of the Fermi National Accelerator Laboratory (FNAL) are presented and discussed. A strong effort to develop new high field superconducting magnets for next generation accelerators is presently going on at FNAL. Within the High Field Magnet Project (HFM), a Short Sample Test Facility (SSTF) has been set up for testing and characterizing superconducting strands to be used for magnet production. The R&D on high critical current density multifilamentary Nb_3Sn strands with low magnetization and small effective filament diameters is an important part of this program, which is pursued by FNAL in collaboration with industry, universities, and other National Laboratories.

Within this framework, a balanced coil magnetometer for the measurement of the magnetic properties of superconducting strands has been set up at the SSTF as a part of this thesis work. This new apparatus has been accurately calibrated and tested, and has allowed to obtain reliable measurements of the strand properties.

Furthermore, significant results have been obtained in characterizing the properties of Nb_3Sn multifilamentary strands produced with the Internal Tin, the Modified Jelly Roll, and the Powder in Tube technologies, in investigating the origin of critical current degradation due to cabling, in exploring how heat treatment affects Nb_3Sn properties, in studying homogeneity of magnetic properties along a Nb_3Sn strand, and finally in demonstrating the independence of the effective filament diameter on magnetic field in Internal Tin Nb_3Sn.

CHAPTER

1

THE TEVATRON AND BEYOND

1.1 INTRODUCTION

A strong effort is presently spent at Fermilab in developing new high field superconducting magnets for next generation accelerators. The vanishing electrical resistance of superconducting coils and their ability to provide magnetic fields far beyond those of saturated iron is the main motivation for the use of superconductor technology in all new large proton, antiproton and heavy ion circular accelerators. Superconductivity does not only open the way to much higher particle energies, but at the same time leads to a substantial reduction of operating costs. Beam energies in the TeV regime are hardly accessible with standard technology, due to the enormous power they would require. The electrical power consumption of an accelerator cryogenic plant may easily be 1-2 orders of magnitude lower than the power needed in an equivalent warm machine of the same energy. In this chapter, the accelerating machines at Fermilab, the laboratory options for future accelerators, and some highlights on superconducting magnets are described.

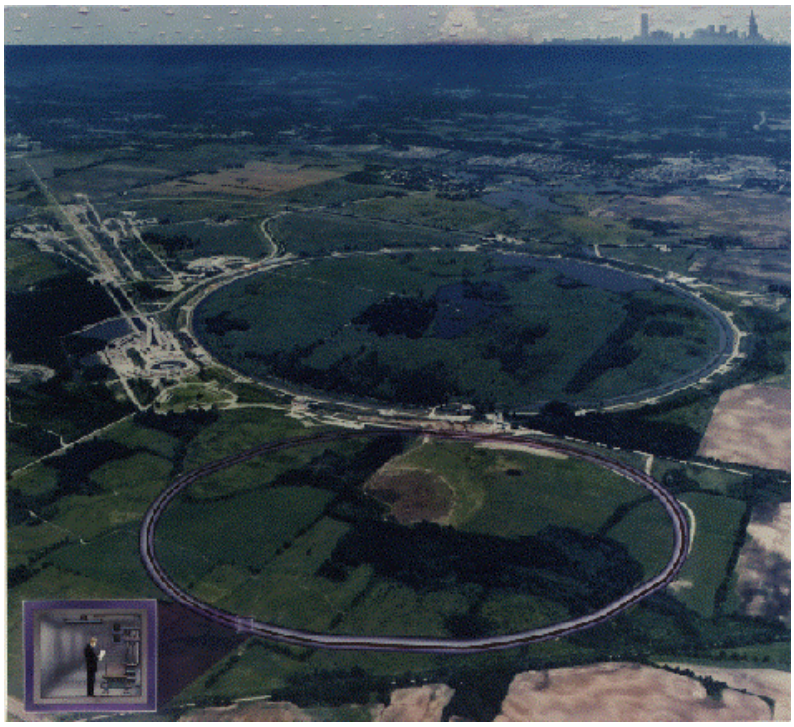

Figure 1.1 Fermilab site.

1.2 HIGH ENERGY ACCELERATORS AND FERMILAB

A discussion of the scientific motivations of the strong effort going on all over the world to build accelerators of higher and higher energy is beyond the scope of this thesis. Still the main themes of today's particle physics are mentioned here below.

1.2.1 Premise

High energy machines are mainly motivated by the need of understanding the origin of symmetry breaking of electroweak interactions of elementary particles, the origin of their masses and of the masses of the force carriers, the reason why matter predominates over anti-matter in the universe. Besides completing our present understanding of the Standard Model, future observations will also hopefully lead to extend the theory and eventually reach the unification of gravity with the other forces. New observations might also lead to understand what is the composition of dark matter in the universe. Most of these searches are

carried out by smashing particles of very high energy into each other, and by analyzing the nature and the characteristics of the new particles produced at the expense of the collision energy. These interactions are obtained either by blasting high momentum particles onto a fixed target or by making them collide head-on among themselves. In head-on colliders, in order to achieve high event rates, the particles are bunched together and the bunches are formatted into high intensity beams. For the deepest studies of particle structures and for the production of more massive new particles, higher and higher energies are needed, and of course the more complex are the accelerators. Accelerators can be divided in two types:

- Linear accelerators;
- Circular accelerators.

In a linear accelerator, charged particles travel along a straight trajectory and go through a number of accelerating stations. An outstanding example is the 45 GeV electron/positron LINAC at SLAC, Stanford University, CA, USA.

In a circular accelerator, the beam is circulated many times in a closed orbit along which a number of accelerating stations are present. Bending magnets and focusing elements are distributed over the accelerator arcs to keep the particles, during acceleration, on the same orbit and within the accelerator acceptance. Beside Fermilab's Tevatron, that will be described in some more detail below, LEP at CERN, Geneva, Switzerland, and HERA at DESY, Hamburg, Germany, are examples of circular accelerators. LEP is an electron-positron collider of maximum energy 101x101 GeV as of today. HERA is a proton-electron collider, whose superconducting proton ring has an energy of 820 GeV, whereas its electron/positron ring has an energy of 28 GeV.

1.2.2 Fermilab and the Tevatron

Fermilab was started in 1967. The first large circular accelerator operating on site was the Main Ring with its injection stages consisting of a proton source, a linear accelerator (LINAC) and a booster ring. The main ring, shown at the center of Figure 1.1, had a circumference of 6.2 km. The proton beam had maximum

energy of 450 GeV, and was ejected and used against fixed targets. A few years later, the Tevatron, the first accelerator made with superconducting magnets, was built in the same tunnel. The main ring served as last injector element to the Tevatron. The proton beam energy doubled to 900 GeV. In 1984, the Antiproton Source became integral part of the Fermilab accelerator complex, allowing the Tevatron to operate as a proton-antiproton collider with a center of mass energy of 1800 GeV. More recently, the Antiproton Recycler, to increase the intensity of the antiproton source, and the Main Injector, to replace the main ring and increase the intensity of the primary proton beam, were built. The latter can be seen in Figure 1.1 in the foreground. The Recycler is presently being tested and will be operative next year for collider Run II, while the Main Injector is operative now in the on going Tevatron fixed target run.

Several stages progressively raise the beam energy. The accelerating steps of the proton beam at Fermilab include (see also Figure 1.2):

- Cockcroft-Walton electrostatic accelerator;
- LINAC;
- Booster;
- Main Injector;
- Tevatron.

For the collider mode of the Tevatron operation, the Main Injector also feeds an antiproton source. The source comprises an external target where antiprotons are generated, a collecting and focusing channel debuncher ring, where single shot antiprotons are collected, an accumulator ring fed by the debuncher, and a recycler ring, where the "old" protons are rescued at the end of a Tevatron collider run.

The Cockcroft-Walton provides the first stage of acceleration. In this device, electrons are added to hydrogen atoms. The resulting negative ions, each consisting of two electrons and one proton, are attracted by a positive voltage and accelerated to an energy of 750 keV. After leaving the Cockcroft-Walton, the negative hydrogen ions enter a linear accelerator called the LINAC. The LINAC consists of five tanks containing sets of drift tubes. An oscillating electric field is

applied to the tubes. The particles travel through the drift tubes in phase with the electric field, shielded by the tubes when the electric field would slow them down, and emerging in the gaps in between the tubes when the field is accelerating. In a recent upgrade the LINAC energy was increased to 400 MeV. After exiting the LINAC, the ions are stripped of their electrons by a carbon foil, resulting in a proton beam that is injected into the Booster synchrotron ring. The Booster accelerates the protons to an energy of 8 GeV, and, via pulsed operation, it organizes the high frequency sequence of LINAC pulses into a smaller number of bunches for injection into the Main Injector. The Main Injector is the most important improvement for Run II. It accelerates alternatively protons and antiprotons, up to 150 GeV for injection in the Tevatron. Alternatively it sends a 120 GeV beam to the antiproton production target. The final stage of acceleration is provided by the Tevatron, a superconducting synchrotron of 1 km in diameter, with bending dipole magnets reaching a 4 T magnetic field. In collider mode, protons and antiprotons are injected separately into the Tevatron, and circulate in the same beam pipe. The acceleration in the Tevatron is provided by a set of RF superconducting cavities. An energy of 900 GeV was reached by the Tevatron beams during Run I. In the future Run II, thanks primarily to an improved cooling system, 1 TeV per beam will possibly be reached.

The luminosity in the Tevatron collider is proportional to the beam currents, the antiproton current being the critical element. A recycler collects the antiprotons survived at the end of the physics run and makes them available for next stores. This recycler ring is made of permanent magnets, and it is located in the same tunnel as the Main Injector. The accelerating chain is quite complex since many machines are used in series. All of them have to be synchronized and must work to specification in order to obtain the optimum beam configuration. Collisions of the beam bunches must occur at the center of the particle detectors surrounding the beam pipe at specific azimuths around the Tevatron ring. The two main detectors operating at the Tevatron Collider are CDF (Collider Detector at Fermilab) and D0. These detectors discovered the Top Quark in 1995.

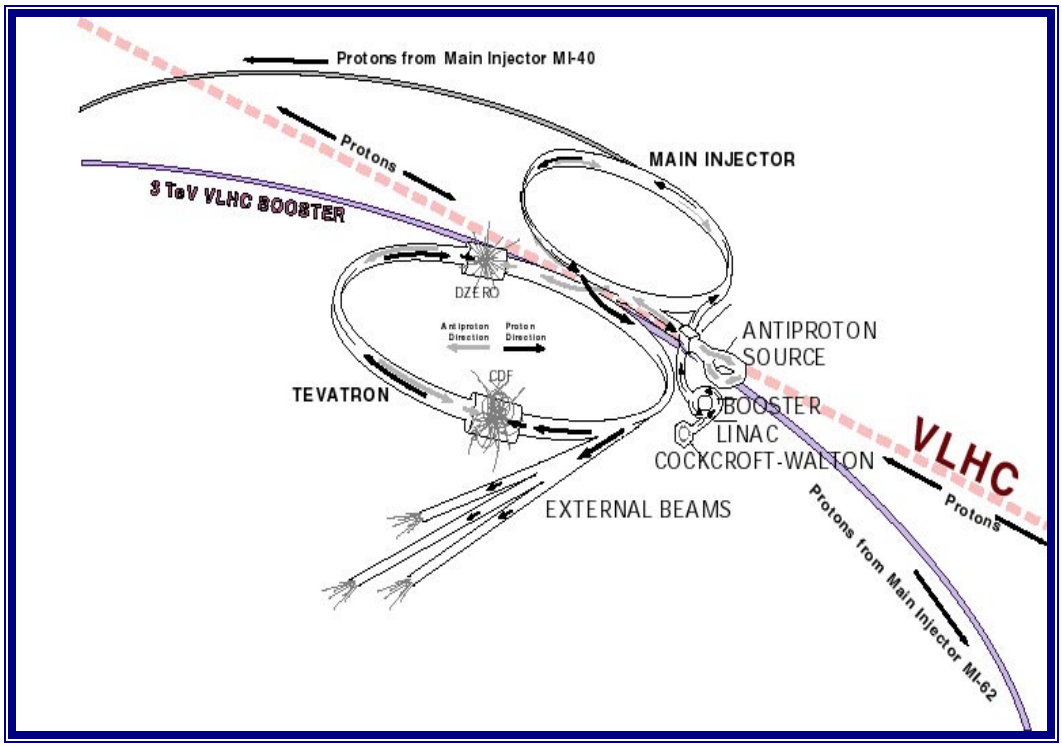

Figure 1.2 Accelerators at Fermilab.

The Tevatron is the highest energy accelerator in the world. Its magnet ring is based on a FODO (focusing-drift-defocusing-drift) cell magnet sequence, where magnets with separated functions are used. For beam bending, superconducting dipole magnets with NbTi technology are used, while superconducting quadrupole magnets provide focusing. This machine will set the energy frontier in the particle physics until approximately 2005, when the new proton-proton Large Hadron Collider (LHC) at CERN will become operative. New much larger and very challenging accelerators are being studied right now in order to extend the research in particle physics beyond the present energy limits.

1.3 NEXT GENERATION MACHINES

In a few years (possibly in 2005), the LHC proton-proton collider at CERN will operate in the same circular tunnel in which LEP is running now. For a given accelerator energy the two parameters that can be adjusted, the radius of the

machine and the field of its magnets, are not independent of each other. The higher the field in the magnets, the smaller is the machine. With a circumference of 27 km and an 8.4 T bending magnetic field, the LHC proton beams will reach a maximum energy of 7 TeV each. Since the LHC collides protons on protons, special "2 in 1" magnets are employed, which accommodate the two separate beams circulating in opposite directions. Being the machine approximately circular, bending radius, bending field, and beam energy are related by the simple relationship:

$$E_{GeV} = 0.3 q B_m r \,, \tag{1.1}$$

where:

q is the particle charge [units of electron charge],
B_m is the bending field of the magnets [T],
r is the radius of the circular accelerator [m].

A fraction of the LHC magnets are being built in the US, and Fermilab is the most important center for the US LHC project. Superconducting NbTi technology was chosen for the LHC magnets, as was done for the Tevatron first and for HERA next, with maximum dipole fields of 4 T and 6 T respectively. The nominal operating field of LHC is 8.4 T. Because of their higher field, the use of superconducting magnets allows for reduction of tunneling costs. However as the field increases, better superconductor properties are required, raising costs again. Superconducting NbTi is a ductile alloy which is ideal for manufacturing composite strands, for making cables out of them, and eventually wind magnet coils. Nevertheless, with an upper critical field (see Chapter 2) of about 11.5 T at 4.2 K, the LHC NbTi coils would have to be pushed near their critical current limits to operate at 8.4 T. A safe operation point was achieved at LHC by lowering the magnet operating temperature to 1.9 K (superfluid helium). At this temperature the NbTi upper critical field rises to 14 T. This choice moved the technological effort more onto the cryogenic system than on the superconducting material R&D.

More cost-effective solutions are presently being studied for a post-LHC Very Large Hadron Collider (VLHC) [1, 2]. At the Snowmass_96 Summer Study on New Directions for High Energy Physics (HEP), a goal was set of a 50 TeV x 50 TeV proton-proton collider with a 3 TeV injector. Fermilab could possibly be the site for the VLHC. Figure 1.2 shows how the new machines could be integrated at Fermilab [3].

At present two main options for the VLHC bending magnets are being pursued, a low field and a high field one. The low field version would be a ring of 600 km in circumference with 2 T transmission line magnets, while the high field version would employ 12 T dipole magnets in a ring of 100 km in circumference. The main advantage of a high field choice would be the enhancement of luminosity, thanks to synchrotron radiation beam damping. This phenomenon becomes important at around 10-12 T. At higher bending the machine luminosity is limited by other effects, while the cooling system is unnecessarily overloaded. The choice between the low and high field options is also determined by the overall construction costs, which are a balance between magnet production and tunneling costs. At present the low field option appears to be of lower cost. Whereas for the low field magnets NbTi can be used, in the case of the high field option other kinds of superconductors have to be considered. Multifilamentary Nb_3Sn is one of the most promising materials. Strand and cable R&D is actively pursued by Fermilab within the High Field Magnet Project (HFM), using different Nb_3Sn technologies and as a benchmark, the strand design developed for the International Thermonuclear Experimental Reactor (ITER).

1.4 SUPERCONDUCTING MAGNETS

Keeping the charged particles confined around a circular orbit requires both bending and focusing forces generated by electromagnetic fields. The Lorentz force is given by:

$$\vec{F} = e\left(\vec{E} + \vec{v} \times \vec{B}\right), \tag{1.2}$$

where :

E is the electric field,

e is the electron charge,

v is the particle velocity, and

B is the magnetic field.

The electric term in equation 1.2 must be used for acceleration, while the magnetic term that does not generate work can only be used for bending. At high energy, where $v=c$, a magnetic field of barely 1 T generates the same Lorentz force as an electric field of $3x10^8$ V/m. Although they do not increase the particle energy, magnetic field are thus very effective in bending the trajectory. Magnetic dipole fields perpendicular to the plane of the particle trajectory are used to bend the beams. Quadrupole fields around the beam axis focus the particles, and longitudinal electric fields are used to accelerate them.

A noticeable difference to be taken into account in comparing a conventional and a superconducting magnet is that in the former the field is present almost only in the iron sector, while in the latter the field surrounds the entire space around it. This configuration significantly constraints the choice of the structural materials.

The focusing lattice most frequently used in a circular accelerator is a series of identical cells, each containing a focusing (F) and defocusing (D) quadrupole magnets separated by drift (O) spaces (FODO lattice). In between the focusing cells are positioned the dipole bending magnets. This structure is called separated function, to distinguish it from systems with integrated functions, where the bending magnets have radial dependent bending field that is also capable of performing the required focusing. Using magnets with separated functions allows greater design and operation flexibility.

The challenging requirements in superconducting magnet design are [4]:

- Field strength. The general rule is the higher the field strength, the better. Not only bending, but also focusing and defocusing is more efficient at higher fields;

- Field quality. Since the beam has to circulate many times around the same orbit, small imperfections in the field decrease the beam lifetime;
- Magnet bore size. The cost of the magnet increases dramatically with the bore size. However, from the point of view of beam acceptance, the larger the bore size, the better it is. At high energy, the beam size can be small but induced fields misalignments and other factors may force to make the acceptance much larger then beam size;
- AC-DC behavior. To keep the particle in orbit during acceleration, the magnets have to be ramped. However at maximum beam energy and in collider mode operation, the field must be very stable for many hours;
- Radiation hardness. The magnet has to survive in a high radiation area for the entire expected life of the machine;
- Reliability. The malfunctioning of a single magnet can cause the loss of the entire beam. With more than one thousand magnets in the ring, this clearly imposes strict reliability requirements on each of them.
- Cost. Because of the large number of magnets, both their production and their maintenance cost should be kept as low as possible.

Despite the anticipated strong saving in operating cost, the introduction of superconducting magnets generated other problems like:

- Persistent eddy currents. Eddy currents in the superconducting filaments are induced during the magnet current ramp. Because of the vanishing resistance of the material, they do not decay and generate dipolar and higher multipolar fields;
- Quench behavior. If one of the critical parameters in the superconductor is exceeded the magnet quenches to the normal resistance state. The machine must be protected from possible damage, and must be able to recover quickly from quenches;
- Cryogenics. An accurate study on the cryogenic plant and transport lines is needed in order to avoid high costs for refrigeration.

In a bending magnet of the high energy machines under consideration, the saggita at the magnet exit is negligible with respect to the magnet length. Therefore the key elements of the magnet design are coil cross section and conductor distribution over it. Given bore size and magnetic field, conductor volume and field quality should be optimized by a careful design of these parameters. Presently the most successful coil design is based on the so called cos(θ) conductor distribution. This solution produces the desired magnetic field with the smallest amount of superconductor. As already mentioned, field quality is also very important. This parameter directly affects beam optics and beam stability. Important sources of field errors are misalignments of the conductor and of the iron yoke on magnet cross section, iron saturation, coil deformation under Lorentz forces, and most of all the superconductor magnetization. Superconductor magnetization is reduced primarily by reducing the superconducting filament diameter. This is one of the challenging goals in superconductor development.

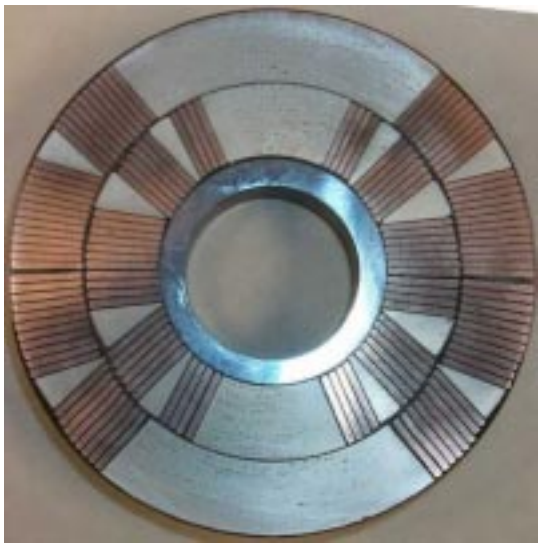

Figure 1.3 Superconductor distribution in a cos(θ) design dipole magnet.

1.5 OTHER APPLICATIONS OF SUPERCONDUCTIVITY

The realization of high field magnets for high energy physics is one of the most fascinating and difficult applications of superconductivity, but there are many other important fields in which superconductors can possibly be used. This is especially true, after the discovery in 1986 of high temperature

superconductors, where T_c is greater than 77 K (liquid nitrogen temperature). Applications and present R&D projects include [5]:

- Magnetic resonance imaging;
- Energy storage;
- Controlled thermonuclear fusion;
- Magnetohydrodynamic power generation;
- DC motors and AC machines;
- Magnetic levitation.

1.5.1 Magnetic resonance imaging

Superconducting magnets are used routinely in many hospitals in magnetic resonance imaging (MRI) applications. In this technique, a magnetic field is used to align the spins of hydrogen atoms (mostly contained in H_2O molecules), and an electromagnetic pulse is then given to excite spin orbit transitions. When the pulse is over, the spins go back to the original state emitting a characteristic electromagnetic wave. The wave can be detected by direction-sensitive sensors and used to create two-dimensional pictures of the human body. MRI is widely used to diagnose tumors, especially in sensitive parts of the body like the brain, where intrusive techniques are risky.

1.5.2 Energy storage

Storage superconducting magnets have been proposed as a large reservoir of energy (Superconducting Magnetic Energy Storage SMES) in order to balance the daily variations in the electricity demand. When the available electric power grid exceeds the demand, the SMES can adsorb and store energy. This electromagnetic energy can be dumped back into the network to satisfy increased demand during the peak hours. A SMES was built within the "Star Wars" US defense program. This kind of application has not been transferred yet to the

civilian field due to the complexity and costs of keeping such large magnets at cryogenic temperatures.

1.5.3 Controlled thermonuclear fusion

Magnetic confinement of hot plasma may be the most promising way to achieve commercial production of power from controlled thermonuclear fusion. Given the extreme confinement fields required, superconducting coils are the only possible choice. The Joule loss of conventional copper magnets would be 100 times greater than the power required for refrigeration. The most advanced project in this field is ITER, a tokamak fusion reactor, shown in Figure 1.4. The magnetic field to confine and stabilize the high temperature plasma is generated by two types of coil systems: toroidal coils and poloidal coils. Fusion reactions take place when the plasma is sufficiently hot and dense, and contained long enough for the nuclei to start fusing together in an energy positive process. This international experiment is supported by Europe, Japan and Russia. USA decided to withdraw from the collaboration in 1998.

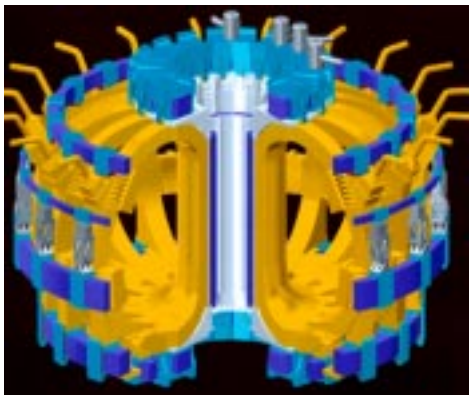

Figure 1.4 ITER design.

1.5.4 Magnetohydrodynamic power generation

Magnetohydrodynamic generation is a technique for the direct conversion of thermal to electrical energy. The principle of this method is based on the induction of an EMF by means of a transverse magnetic field in a hot gas flow, and subsequent extraction of a DC power. The purpose of using superconducting magnets is the same as for the fusion reactors, the energy produced has to exceed the power input. This technology will possibly become of commercial interest

before thermonuclear fusion, contributing significantly to fossil fuel energy saving.

1.5.5 DC motors and AC machines

The superconducting technology applied to electric motors would allow to reduce sizes and to reach higher efficiency. The advantages are most evident in big motors, especially those for marine propulsion. The hardest problem is to build a rotating cryostat, and to transmit the torque between zones at room and at low temperature. The same problem has to be solved as for AC generators. In this case, the design of a cryostat rotating at 50-60Hz with a high centrifugal acceleration of some 5000g rises many technical problems. In the last years, several prototypes of DC motors have been built, but none of them is working reliably. A prototype for a 300 MVA superconducting generator is now under construction by Westinghouse Electric Corporation in USA.

1.5.6 Magnetic levitation

One of the most fascinating applications of superconductivity is magnetic levitation. The idea of designing vehicles floating on magnetic fields is not new, but the introduction of superconducting magnets made it approachable, by means of high magnetic fields, low weights, and low energy consumption. Magnetic levitation applied to train transport is especially pushed in Japan. Some prototypes have already been built, and a record speed of 577 km/h has been reached. The advantages of these vehicles are high speeds, no contact with the ground, no moving parts, and no noise.

1.6 SUMMARY

In summary, the advantages of a superconducting circular accelerator are that the magnetic field can be greatly increased, with a reduction in the ring diameter, and a greatly reduced power consumption.

The main requirements for superconducting magnets in particle accelerators are high field uniformity and low cost. For the former, composite wires with very fine filaments are needed to reduce their magnetization and the associated field error. To reduce the cost, the critical current density should be pushed ad high as possible.

CHAPTER

2

SUPERCONDUCTIVITY

2.1 INTRODUCTION

Superconductivity is a discovery of the 20th century. A Dutch physicist, Heike Kamerlingh Onnes, first saw this phenomenon in 1911. Since 1882, Onnes had been working on the science of cryogenics to liquefy gases. He wanted to check the Van der Waals law describing the behavior of a real gas. In 1908, he succeeded in liquefying helium at 4.2 K and atmospheric pressure. This occurred almost 10 years after hydrogen liquefaction (by James Dewar), due to the technological difficulties in bringing temperature down from 20 K to 4.2 K. This achievement was important because the boiling point of helium is extremely stable, allowing many low temperature experiments simply by immersing the device in a helium bath [6].

Onnes understood this opportunity, and decided to investigate the electrical resistance in metals at liquid helium temperature. It was generally thought that the resistance in a metal decreases with temperature, but what exactly happened approaching absolute zero was hotly debated. Lord Kelvin believed that the electron flow would stop, raising the resistance to infinite, while Onnes and Dewar assumed that the resistance would fall with temperature, ultimately

reaching zero. What really happens in normal metals at low temperature is that even close to zero temperature, the resistance remains finite because of impurities and dislocations of the metal lattice. This was unpredictable at that time, but what Onnes was about to discover was even more astonishing. To avoid the effect of impurities, Onnes used mercury, which could be distilled, thanks to its liquid state at room temperature. After immersion in boiling helium, the electrical resistance dropped suddenly to zero at a temperature T^* in the vicinity of 4 K [7]. What surprised the researchers was how fast the phenomenon occurred. The experiment was repeated several times to avoid any doubt on its reproducibility. Finally Onnes reported that "the material, below a critical temperature, passed into a new state, which on account of its extraordinary electrical properties could be called the superconducting state". A copy of the original plot is shown in Figure 2.1. On the basis of modern equipment sensitivity, the resistivity of superconductors is found to be less than 10^{-26} Ω·m. For comparison, the resistivity of high purity copper is of the order of 10^{-11} Ω·m.

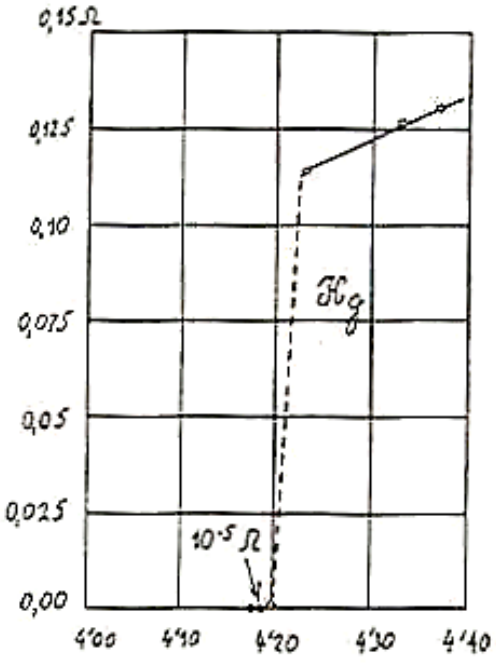

Figure 2.1 The experiment of H. K. Onnes.

In 1913, Onnes won the Nobel Prize for liquefaction of helium and the discovery of superconductivity. Other metals like tin, lead, indium, aluminum, and niobium, and many alloys and intermetallic compounds also turned out to be superconductors. The temperature of the transition from the normal to the superconducting state was called the critical temperature, T_c.

Soon after, it was found that at a given temperature, either a magnetic field in excess of what was called critical magnetic field, B_c, or a current in excess of a critical current,

I_c, could destroy the superconducting state. The independent parameters T_c, B_c, and I_c are used to define the critical surface of the superconducting state, as shown in Figure 2.2.

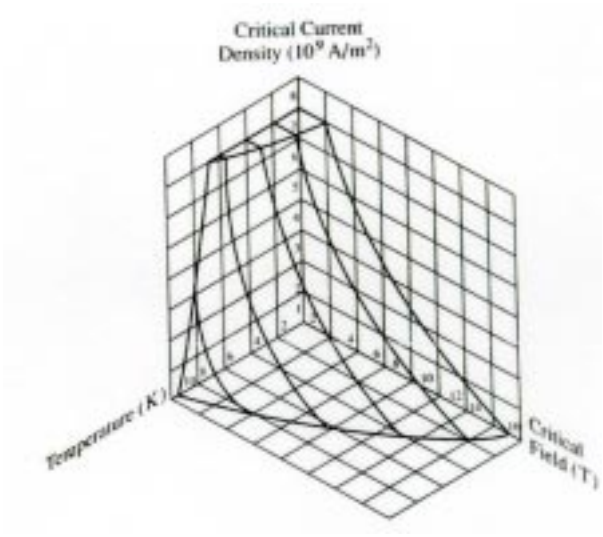

Figure 2.2 Critical surface for NbTi.

In the following years, the technological development in cryogenics allowed to better study superconductors. W. Meissner and R. Ochensfeld made a significant discovery in 1933 [8]. They proved that in a weak external magnetic field, a superconductor completely expels the magnetic flux from its interior, and that the zero induction is an intrinsic property of the superconducting state. This also implied that the transition to the superconducting state could be treated as a phase transition.

Magnetic field expulsion is known as Meissner-Ochsenfeld effect, and was modeled by F. London two years later by introducing two equations in addition to Maxwell's equations [9,10]. Although London's phenomenological two-fluid model correctly described absolute diamagnetism and zero resistance to a dc current, it did not attempt to resolve the microscopic mechanism of superconductivity at the level of electrons, that is, to answer the question "Why?". Moreover, it always predicted that the energy required to create the interface between adjacent normal and superconducting regions was negative (*i.e.* negative surface energy, σ_{ns}), against experimental evidence.

The above contradiction was reconciled by a theory proposed in 1950 by V. L. Ginzburg and L. D. Landau, which was phenomenological, but took into account also quantum effects [11, 12]. Its breakthrough was to assign a unique wave function to the entire ensemble of superconducting electrons, thus

establishing their coherent behavior. This idea enabled the prediction of many beautiful macroscopic quantum effects in superconductivity.

In 1957, by applying the Ginzburg-Landau theory to superconducting alloys, A. A. Abrikosov developed a theory of the so-called type II superconductors [13]. It turned out that superconductors can be divided in type I and, II according to their σ_{ns} being respectively positive or negative. To this latter category belong most superconducting alloys and chemical compounds, as for example brittle intermetallics with the A15 crystal structure. After the Meissner phase, type II superconductors allow flux penetration inside the material in the form of quantized vortex lines, allowing superconductivity up to very high fields (called upper critical field, B_{c2}). The applications of type I superconductors is of less interest, as mentioned below.

Still no theory could yet explain “What were those superconducting electrons?”. This question was finally answered in 1957 by the microscopic theory of superconductivity of J. Bardeen, L. Cooper and J. Schrieffer, known as BCS theory [14]. This theory is based on the assumption that the supercurrent is not carried by single electrons, but by pairs of electrons, of opposite momenta and spins, attracted by the interaction between electrons and phonons. These so-called *Cooper pairs* obey Bose-Einstein statistics and they all occupy the same ground state as a dissipation-free superfluid.

In 1971, the Chevrel-phase compounds were discovered. Ternary molybdenum sulfide $PbMb_6S_8$ had a critical temperature of 15 K and an upper critical field of 60 T.

A new push in the field was given in 1986 by the K. A. Muller and J. G. Bednorz's discovery of the first high T_c superconductor, a lanthanum, barium, copper and oxygen ceramic ($LaBaCuO_4$) that reached a critical temperature of about 40 K. For this discovery they won the Nobel Prize in 1988. New enthusiasm was stirred into the scientific community, that lead to Paul C. W. Chu and Maw-Kuen Wu's synthesis of $YBa_2Cu_3O_7$, with a T_c of 95 K [15]. For the first time, superconductivity was found to exist at temperatures above 77 K (boiling

liquid nitrogen), opening the opportunity to cheaper cooling systems and, maybe, to commercial applications.

2.2 MEISSNER EFFECT AND LONDON EQUATIONS

The behavior of a superconductor in an external magnetic field was thoroughly investigated by Meissner and Ochsenfeld in the 1930s. They performed an experiment (scheme shown in Figure 2.3) in which a tin cylinder was first cooled under T_c, and next placed in a magnetic field which was made to rise from zero up to a certain value B_0. A surface current was induced in the sample, whose magnetic field, according to Lenz law for an ideal conductor with electrical resistivity ρ=0, exactly cancelled the applied field in the interior. Keeping the external field constant, the current kept flowing in the material, whose interior was flux free, reproducing a perfect diamagnetic state. The experiment was then replayed with an inversion of the two operations. The sample was first placed at room temperature in an external magnetic field B_0, and next cooled down. Above T_c, the magnetic field penetrated its bulk, but below T_c, a surface current was generated and the magnetic field was expelled from the

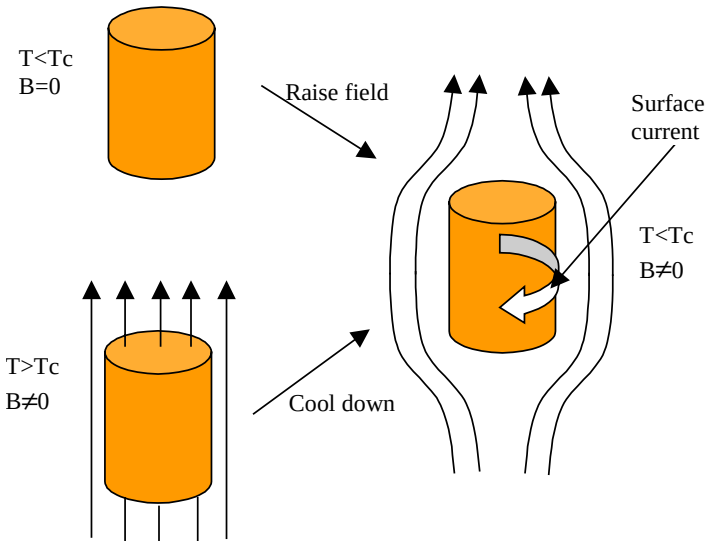

Figure 2.3 Meissner- Ochsenfeld effect.

interior of the material. Lenz inductive law could explain only the first case, but not the second, since the field had been kept constant. This proved that the superconductor was not simply an ideal conductor, since the field inside the specimen was always zero, independent of the specimen's history. In formulae:

$$\vec{B} = \vec{B}_0 + \mu_0 \vec{M} = 0. \tag{2.1}$$

Fritz London gave a description of the phenomenon dividing all free electrons (of charge *e* and mass *m*) in the superconductor into two groups: *super-electrons* of density n_s which generate supercurrents with zero resistivity, and normal electrons of density n_n [10]. The total density n is the sum of n_s and n_n. As the temperature increases from 0 to T_c, the density n_s decreases from n to 0. The equation of motion for superconducting electrons in an electric field is:

$$n_s m \dot{\vec{v}}_s = n_s e \vec{E}, \tag{2.2}$$

where:

v_s is the superfluid velocity;

E is the electric field.

Taking into account that the supercurrent density, J_s, is:

$$\vec{J}_s = e n_s \vec{v}_s, \tag{2.3}$$

one obtains the first London equation:

$$\dot{\vec{J}}_s = \frac{n_s e^2}{m} \vec{E}. \tag{2.4}$$

This equation describes the resistanceless property of a superconductor, since in stationary conditions there is no electric field generated in the superconductor.

Applying the curl operator to both members of equation 2.4, the 3rd Maxwell equation:

$$\nabla \times \vec{E} = -\frac{\partial}{\partial t} \vec{B}, \tag{2.5}$$

can be written as:

$$\frac{d}{\partial t}\left(\frac{m}{n_s e^2}\nabla\times\vec{J}_s+\vec{B}\right)=0. \tag{2.6}$$

According to the classical theory of electromagnetism, the expression in the brackets is a constant. The new assumption made by London was that in the superconducting state, this constant is equal to zero, yielding:

$$\nabla\times\vec{J}_s=-\frac{n_s e^2}{m}\vec{B}. \tag{2.7}$$

This is second London equation, which describes perfect diamagnetism. Taking into account the 4th Maxwell equation:

$$\nabla\times\vec{B}=\mu_0\vec{J}_s, \tag{2.8}$$

equation 2.7 becomes:

$$\nabla^2\vec{B}-\frac{1}{\lambda^2}\vec{B}=0, \tag{2.9}$$

where:

$$\lambda=\sqrt{\frac{m}{\mu_0 n_s e^2}}. \tag{2.10}$$

Equation 2.9 can be obtained in a more sophisticated way that implies no assumptions, by solving a variational problem, namely by finding the function **B(x)** corresponding to the minimum value of the superconductor free energy [16].

In the case of a superconducting semispace x>0, whose surface coincides with the plane x=0, in the presence of a magnetic field oriented along the y axis, equation 2.9 can be written as:

$$\frac{d^2B_y}{dx^2}-\frac{1}{\lambda^2}B_y=0, \tag{2.11}$$

whose solution is:

$$B_y(x) = B_0 \exp(-x/\lambda), \tag{2.12}$$

with the boundary conditions: $B(0) = B_0$, $B(\infty) = 0$.

According to this model, the magnetic field does not drop abruptly to zero at the boundary of the superconductor, but penetrates in the material with an exponential attenuation. The characteristic decay length is λ, called London Penetration Depth. It follows from equation 2.8 that the supercurrent at the surface falls off over the same length. Typical values for λ are 20-100 nm. This behavior is typical of type I superconductors, and it strongly limits their application.

2.3 THERMODYNAMIC PROPERTIES

The transition from the perfectly diamagnetic superconducting state to the non-magnetic normal state is a *reversible* transition, in the thermodynamic sense. Thermodynamic arguments can therefore be applied to a superconductor, using the temperature T and the magnetic field B_0 as thermodynamic variables.

2.3.1 Thermodynamical critical field

The value of the critical magnetic field can be derived by studying the effect that an applied magnetic field B_0 has on the free energy of a superconducting specimen. In any system, the stable state is that with the lowest free energy. The relevant quantity to be used in the comparison of the free energies of the superconducting and normal phases is Gibbs free energy density, g:

$$g = u - Ts + pv - B_0 M, \tag{2.13}$$

where u is the internal energy density, s the entropy density, v the specific volume, p the pressure, and M the magnetic dipole moment per unit volume.

Consider a long cylinder of superconductor. In the absence of a magnetic field, let the Gibbs free energy per unit volume of the superconducting state be $g_s(0)$ and that of the normal state be $g_n(0)$. When a magnetic field B_0 is applied parallel to the cylinder axis, at constant pressure and temperature, the superconductor free energy density changes by:

$$\Delta g_s(B_0) = -\int_0^{B_0} M(B')dB' = \frac{B_0^{\,2}}{2\mu_0}, \tag{2.14}$$

where $M = -B_0/\mu_0$, since magnetization exactly cancels the flux due to the applied field (see equation 2.1). For a superconductor of volume V, Gibbs free energy G_s at a field B_0 can be written:

$$G_s(B_0) = G_s(0) + \frac{B_0^{\,2}}{2\mu_0}V. \tag{2.15}$$

On the contrary, the free energy G_n of a metal in the normal state is constant with B_0. The *critical field*, B_{cm}, is achieved when the free energy in the superconducting state, G_s, equals the free energy in the normal state, G_n:

$$\frac{B_{cm}^{\,2}}{2\mu_0}V = G_n - G_s(0), \tag{2.16}$$

Figure 2.4 illustrates the equilibrium point between these two states. $G_n - G_s(0)$ can be interpreted as the Cooper pair condensation energy (see next section). B_{cm} is called thermodynamical critical field. For type I superconductors, it coincides with B_c, while in the type II case it lies between B_{c1} and B_{c2}.

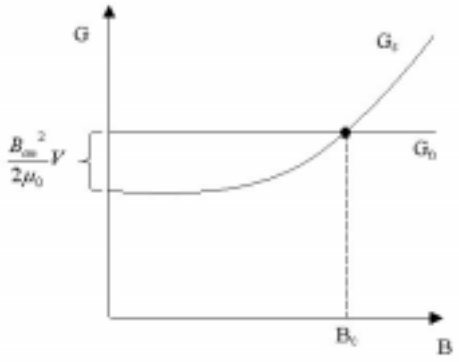

Figure 2.4 Free energy as a function of applied field.

2.3.2 Superconductivity as a phase transition

At constant pressure and constant applied magnetic field, the entropy per unit volume is given by:

$$s = -\left(\frac{\partial g}{\partial T}\right)_{p,B_0}, \tag{2.17}$$

From equations 2.15 and 2.16, one can write:

$$g_n - g_s(B_0) = \frac{1}{2\mu_0}(B_{cm}{}^2 - B_0{}^2), \tag{2.18}$$

Therefore:

$$s_n - s_s = -\frac{B_{cm}}{\mu_0}\frac{dB_{cm}}{dT}, \tag{2.19}$$

The right-hand side of this equation must be positive since dB_{cm}/dT is always negative. This shows that the entropy of the superconducting state is less than that of the normal state, *i.e.* the superconducting state has a higher degree of order than the normal state, in agreement with the BCS theory that predicts a highly correlated system of condensed electron pairs.

With zero applied magnetic field, the transition occurs at the critical temperature. At $T = T_c$, $s_n = s_s$ since B_{cm} falls to zero. This can be written as:

$$\left(\frac{\partial g}{\partial T}\right)_n = \left(\frac{\partial g}{\partial T}\right)_s, \tag{2.20}$$

A phase transition where not only g but also $\partial g/\partial T$ is continuous is known as a second-order phase transition. This implies two important characteristics. At the transition there is no latent heat, and there is a jump in the specific heat, c. The former follows from $dq = Tds$, the latter from the discontinuity of $\partial^2 g/\partial T^2$, whereas $c = -vT\partial^2 g/\partial T^2$.

However, in the presence of an applied magnetic field, the transition occurs at some lower temperature, where $B_{cm} > 0$. In such a case, the entropy of the normal state is greater than that of the superconducting state and latent heat is present. Heat must be supplied if the transition is to take place at constant temperature. In this case, g is continuous, but $\partial g/\partial T$ is not, and the superconducting-normal transition is of the first-order.

2.3.3 Type II superconductors

The discovery of type II superconductors opened the way to applications. This class of superconductors includes several alloys and element niobium (on the boundary between the two types). Type II conductors are characterized by two critical fields, B_{c1} and B_{c2}, both temperature dependent. For external fields between zero and B_{c1}, the substance is in the Meissner phase. Between B_{c1} and B_{c2} the material enters the *mixed phase*, where part of the magnetic flux penetrates the bulk in the form of quantized flux tubes. Above B_{c2}, the material is normal conducting. The difference in magnetization behavior of type I and type II superconductors is clearly shown in Figures 2.5a) and b). In both cases, the area under the curve is the free energy difference between the normal and the superconducting state.

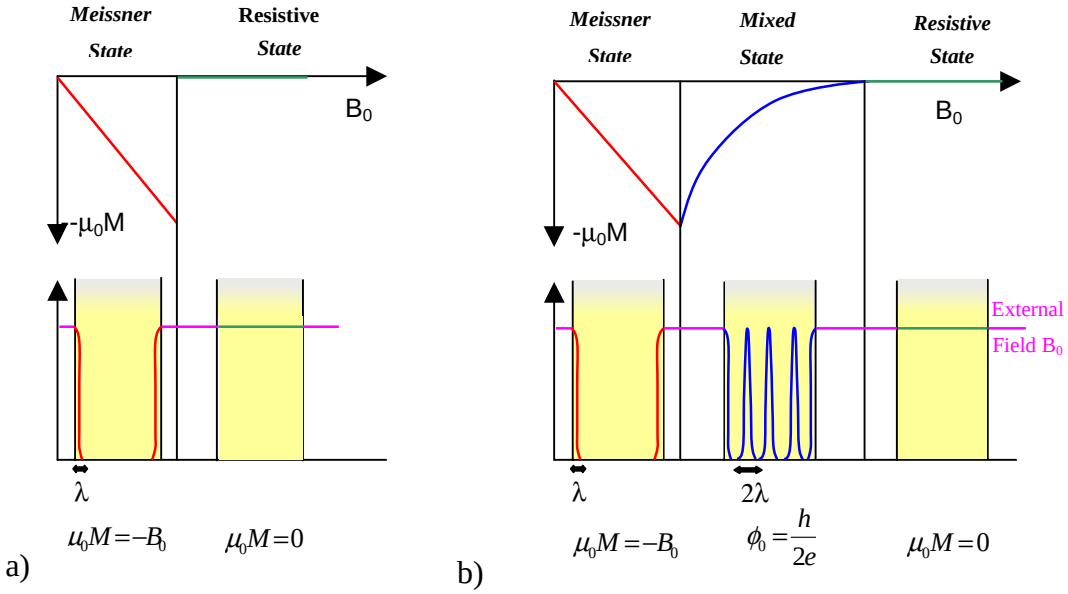

Figure 2.5 Superconductor type I (a) and II (b).

Figure 2.5a shows a type I behavior. In the (B_0, $\mu_0 M$) plane, the Meissner state is represented by a line with a slope equal to –1 that suddenly drops to zero at B_c, when the transition to the resistive state occurs.

Figure 2.5b shows a type II behavior. The Meissner phase is shorter, but at B_{c1} the external field starts penetrating inside the bulk, and the magnetization drops smoothly to zero at B_{c2}.

It is energetically favorable for a bulk superconductor to subdivide itself into an alternating sequence of normal and superconducting slices (*i.e.* mixed state behavior in type II superconductors) to have a negative surface energy.

At the boundary between the normal and the superconducting state, the Cooper pair density does not jump abruptly from zero to its value in the bulk, but rises smoothly over a finite length ξ, called *coherence length*.

In a conductor of unit area, exposed to a field B_{cm} parallel to its surface, the energy balance is as follow:

- The magnetic field penetrates a depth λ into the sample which corresponds to an energy gain since magnetic energy must not be driven out of this layer:

$$\Delta E_{mag} = \frac{B_{cm}{}^2}{2\mu_0}\lambda. \tag{2.21}$$

- On the other hand, because of the Cooper pair density rising over a length ξ, there is a loss in condensation energy:

$$\Delta E_{cond} = -\frac{B_{cm}{}^2}{2\mu_0}\xi. \tag{2.22}$$

There is a net energy gain if $\lambda > \xi$. The Ginzburg-Landau theory gives a more refined treatment of the phenomenon. The Ginzburg-Landau parameter is introduced as follows:

$$\kappa = \lambda/\xi\,, \tag{2.23}$$

and the criterion for type I or II superconductivity is found to be:

Type I	$\kappa < 1/\sqrt{2}$
Type II	$\kappa > 1/\sqrt{2}$

The coherence length is proportional to the mean free path of the conduction electrons in the metal. In alloys the mean free path is much shorter than in pure metals so they are always type II superconductors.

Material	Type	λ [10^{-9}m]	ξ [10^{-9}m]
Indium (In)	**I**	**24**	**360**
Lead (Pb)	**I**	**32**	**510**
Tin (Sn)	**I**	**30**	**170**
Niobium (Nb)	**II**	**32**	**39**
NbTi	**II**	**300**	**5**
Nb_3Sn	**II**	**65**	**3**

Table 2.1 Penetration Depths and coherence lengths of typical type I and II superconductors.

2.4 COOPER PAIRS AND BCS THEORY

Cooper first introduced the concept of superconducting electron pairs in 1956. In the superconducting state, electrons of opposite momenta and spins are bound into pairs. This is possible thanks to the shielding of Coulomb repulsion by the positive ions in the metal. When the first electron moves through the metal lattice, it attracts positive ions, but because of its inertia, the response of the lattice is not immediate. The shortest response time corresponds to the highest possible lattice frequency, which is called Debye frequency, ω_d. The maximum lattice deformation lags behind the electron by a distance, d:

$$d \approx v_f \frac{2\pi}{\omega_d} \approx 100 - 1000\,\text{nm}, \tag{2.24}$$

where v_f is the Fermi velocity which is on the order of 10^6 m/s. The second electron is attracted by the positive ion accumulation in the lattice deformation and the strongest effect is achieved when the two electrons follow adjacent tracks in the lattice and their distance is equal to d. This explains why a Cooper pair is a very extended object. As a consequence, Cooper pairs overlap each other, so that in the space occupied by a Cooper pair there are millions of others. This is very important for the BCS theory because the Cooper pairs must change their partners frequently in order to provide continuous binding. The binding energy of the Cooper pairs is very small, 10^{-4}-10^{-3} eV, so that the pairs can only exist at low temperatures where this energy is not overcome by thermal agitation. Because of their space extension, Cooper pairs differ considerably from other Bosons such as helium nuclei. They only exist in the BCS ground state and

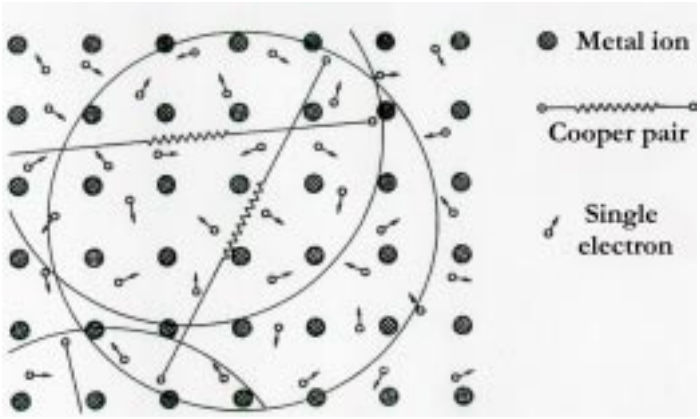

Figure 2.6 Cooper pairs

there is no excited state. An excitation is equivalent to breaking them up into single electrons. The BCS ground state is characterized by a macroscopic wave function and a ground state energy that is separated from the energy levels of the unpaired electrons by an energy gap of 2Δ. This gap is temperature dependent and at T = 0 it can be related to the critical temperature, T_c, trough the following equation:

$$\Delta(0) = 1.76 k_B T_c, \tag{2.25}$$

where k_B is the Boltzmann constant. Both Δ and T_c are proportional to the Debye frequency which in turn is inversely proportional to the square root of the atomic mass, *M*.

2.5 MAGNETIC FLUX QUANTIZATION

Both the BCS and the London theory make the prediction that the magnetic flux trapped in the hole of a superconducting ring does not assume an arbitrary value, but it is quantized. The BCS flux quantum is:

$$\Phi_0 = \frac{h}{2e}, \tag{2.26}$$

i.e. the Plank's constant divided by the charge of the supercurrent carriers. The London flux quantum is twice as big because the charge carriers in the London theory are single electrons. This phenomenon was experimentally proved in 1961 by Doll and Nabauer in Munchen and by Deaver and Fairbank in Stanford, almost simultaneously.

Abrikosov predicted that a magnetic field penetrates a type II superconductor in form of flux tubes or *fluxoids*, each containing a single elementary quantum Φ_0. The fluxoids arrange themselves in a triangular pattern to minimize the potential energy related to their mutual repulsion. The magnetic

field lines are surrounded by a supercurrent vortex. The Cooper pair density drops to zero at the center of the vortex, so the core of a flux tube is normal conducting.

The area occupied by a flux tube is roughly $\pi\xi^2$. When an external field B_0 is applied, fluxoids keep moving into the specimen until their average field is identical to B_0. The fluxoid spacing in the triangular lattice is in this case:

$$d = \sqrt{\frac{2\Phi_0}{\sqrt{3}B_0}}, \tag{2.27}$$

which amounts to 20 nm at 6 T. The upper critical field of a type II superconductor is reached when the current vortices of the fluxoids start touching each other, at which point superconductivity breaks down. In the Ginzburg-Landau theory the upper critical field is given by:

$$B_{c2} = \frac{\Phi_0}{2\pi\xi^2}. \tag{2.28}$$

The experimental observation of the fluxoid pattern was first performed by Essmann and Trauble. They used a lead-indium sample, cooled by liquid helium at 1.2 K. The liquid did not cover the upper surface of the sample. Iron was evaporated at some distance from the superconductor and in the 0.8 mbar helium atmosphere the iron atoms agglomerated to tiny crystals that were attracted by the magnetic field lines and stuck to the sample where the fluxoids emerged. After warming it up, a thin film was sprayed on the surface to allow the iron to be removed for observation in an electron microscope. The observation of the iron agglomerates showed a perfect triangular lattice as predicted.

2.6 HARD SUPERCONDUCTORS

2.6.1 Flux pinning

Despite their superconducting state, ideal type II superconductors show heat generation when carrying a transport current. This is due to *flux flow resistance*. The current exerts a Lorentz force on the flux lines and causes them to move perpendicularly to the current and to the field. To prevent such viscous motion, fluxoids have to be captured at *pinning centers* like defects or impurities in the crystal lattice. Imperfections larger than the coherence length are needed to pin vortices. Pinning is necessary for high J_c's and at present a large effort is spent in finding new ways to increase the pinning center density in Nb_3Sn.

For a superconducting slab in the yz plane with a transport current density along z and an external field along y, 4th Maxwell equation reads:

$$\frac{\partial B_y}{\partial x} = \mu_0 J_z , \tag{2.29}$$

which implies that a non-vanishing current density inside the conductor is necessarily coupled with a gradient in magnetic flux density. Such a gradient can only be maintained if flux pinning exists.

A type II superconductor with strong pinning is called *a hard superconductor*.

2.6.2 Magnetization of a hard superconductor

Hard superconductors exhibit a strong magnetic hysteresis, which is the origin of the persistent-current multipoles in superconducting accelerator magnets. While an ideal type II conductor without any flux pinning should show a completely reversible response to an external magnetic field, a hard superconductor is only reversible in the Meissner phase because then no magnetic field enters the bulk, so no flux pinning can happen. Above B_{c1} magnetic flux enters the sample and is captured at pinning centers. When the field is reduced again these flux lines remain bound and the specimen keeps a frozen-in

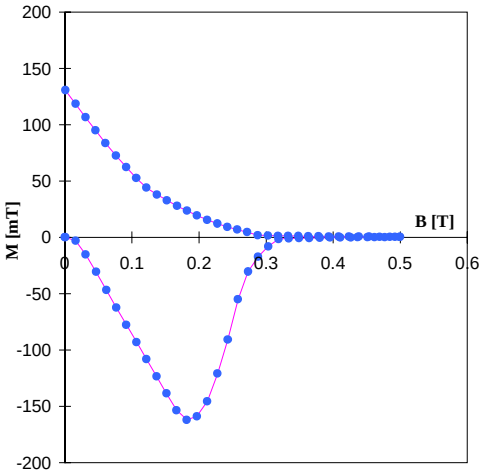

Figure 2.7 Nb hysteresis curve.

magnetization even for vanishing external field. The field polarity has to be inverted to achieve M = 0, but the initial state can only be recovered by warming up the specimen to destroy superconductivity and release all pinned flux quanta. A typical hysteresis curve is shown in Figure 2.7 for a Nb alloy.

2.6.3 Critical state model

Starting from the observation that the resistivity of a hard superconductor is almost a step function of current density, C. P. Bean (1962, 1964) proposed the so-called *critical state model*, according to which there are only two possible states for current flow in a hard superconductor [17]. The current density is either zero or equal to J_c. The Meissner phase is ignored. The critical state model has proved very successful in describing the magnetization of hard superconductors.

For an unmagnetized superconducting slab in the yz plane exposed to a magnetic field along y, 4th Maxwell equation can be written as follows:

$$\frac{\partial B_y}{\partial x} = \mu_0 J_c, \tag{2.30}$$

Up to some small value of B_0, a bipolar current of density $\pm J_c$ is induced in the slab which penetrates to the depth necessary for the shielding field to cancel the applied field in the central region. In the region of current flow the magnetic field is linear, as shown in Figure 2.8a).

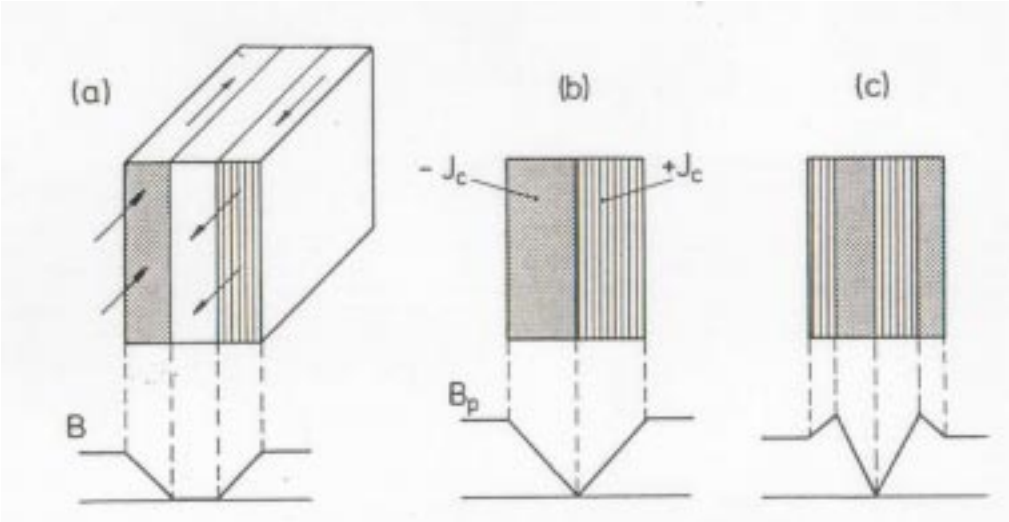

Figure 2.8 Current and field distribution in a slab of hard superconductor according to the critical state model.

As long as the external field is kept constant the current pattern will persist. When the external field is increased, both current and field penetrate deeper into the slab until the center is reached (Figure 2.8b). The associated field is called the *penetrating field* B_p. Raising B_0 beyond B_p leads to a non-vanishing field at the

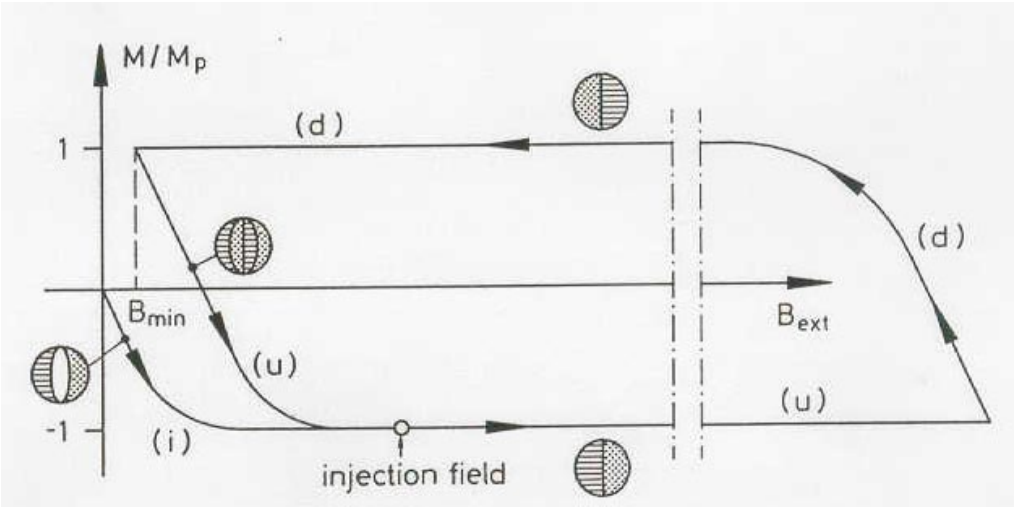

Figure 2.9 The normalized magnetization M/M_p as a function of the external field. (i): initial curve, (u) up-ramp branch, (d): down-ramp branch.

center, but eventually the current density will drop because it depends on magnetic field.

When B_0 is lowered again, a new bipolar current of opposite polarity is induced and the current-field pattern inside the slab assumes the complicated shape sketched in Figure 2.8c). It is straightforward to derive a hysteresis curve from this model (see Figure 2.9). Further details on hysteresis curves will be given in Chapter 7.

CHAPTER

3

SUPERCONDUCTING MATERIALS

3.1 INTRODUCTION

An important issue for the development of new superconducting materials is to reach higher operating temperatures in order to reduce the cost of the cooling system. However, at present only low temperature superconductors (LTS), operating at boiling helium temperature, are used to design and produce magnets, because the main demand on high current densities limits the choice of the material to be used. The new high temperature superconductors (HTS) still do not reach very high current densities and are difficult to produce in the form of long thin wires [18].

The same request excludes using type I superconductors, where in the Meissner state current can flow only in a small part of the strand cross section (delimited by the λ length) near the boundaries. Furthermore, these materials show a very low critical field, which limits applications.

Hard type II superconductors are the only materials usable to manufacture magnets. Among them, only NbTi has been extensively adopted, whereas Nb_3Sn is being produced in smaller quantities. They are known as technical superconductors.

NbTi has undergone development during the last 20 years, and it is generally thought that it has reached its performance limits. It is currently the most commonly used material in magnet industry, but its properties are adequate only up to fields of 8-9 T [19]. MRI solenoids and superconducting accelerators, starting from the Tevatron, HERA, and more recently LHC have relied on NbTi. In addition, the Superconducting Super Collider (SSC), a U.S. project that was first approved and later cancelled, planned to use NbTi. Significant advances in performance as well as conductor cost reduction resulted from the SSC R&D.

For magnets above 10 T, the only appropriate superconductors are A15 and HTS materials that require a new approach to magnet design and fabrication. To form these brittle strain sensitive compounds, high temperature heat treatments are needed. These materials are Nb_3Sn and Nb_3Al (A15), and Bi-2223, Bi-2212, and YBCO (HTS). As already mentioned, HTS's are not competitive yet. On short-term magnet production, Nb_3Sn appears to be the right choice, while Nb_3Al is the most promising on the medium term, showing less strain sensitivity. Nb_3Sn requires heat treatment temperatures of 650-700 C that are acceptable for both the fiberglass insulation and the structural materials. This compound has potential applications at 20 T [20] with a B_{c2} as high as 28 T. Present Nb_3Sn studies focus on increasing J_c, decreasing d_{eff}, and reducing manufacturing costs.

3.2 FILAMENTARY COMPOSITES

The conductor used in magnet industry is not pure superconducting material. Thin filaments of NbTi or Nb_3Sn are embedded in a copper matrix to form a multifilamentary strand. This procedure is necessary to achieve the requirements for magnets. Thin filaments are necessary to:

- prevent flux jumping,
- reduce persistent currents due to magnetization.

Flux jumping is a magnetic instability that can break superconductivity down by releasing the magnetic flux bundles from their pinning centers. It can be explained by considering a thermally isolated superconducting slab of width 2*a* exposed to a vertical external field B_0 larger than the penetrating field B_p. As seen in Section 2.5, a bipolar current of density $\pm J_c(B_0, T_0)$ is induced in the slab, whereas the magnetic field exhibits a linear behavior, with a non-vanishing value at the center. If an amount of heat δQ per unit volume is introduced in the sample, the temperature will rise from T_0 to $T_0 + \delta T$ and J_c will drop by δJ_c. Magnetic flux will then increase, generating heat, which in turn raises the temperature, and so on. The additional energy input due to the Joule heating is equivalent to a reduction in heat capacity [18]:

$$\gamma C_{eff} = \gamma C - \frac{\mu_0 J_c^2 a^2}{3(T_c - T_0)}, \tag{3.1}$$

where:

- γ is the material density,
- C_{eff} is the effective specific heat,
- C is the specific heat,
- J_c is the critical current density,
- a is the slab half-width,
- T_c is the critical temperature at B_0 field, and
- T_0 is the operating temperature.

When C_{eff} vanishes, a small initial perturbation can start a divergent loop causing the temperature to rise until the resistive state is reached. It does not necessarily lead to a quench since the specific heat of the conductor increases with the third power of temperature. To prevent flux jumps, the thickness of the slab must fulfill the inequality:

$$2a \le 2\sqrt{\frac{3\gamma C(T_c - T_0)}{\mu_0 J_c^2}}. \tag{3.2}$$

In the above considerations, the cooling by the surrounding helium has been neglected, and relation 3.2 is called *adiabatic* flux jump stability criterion. To adapt this criterion to multifilamentary strands embedded in a low resistive matrix, some assumptions have to be made:

- The heat pulse in the material is fast enough for adiabaticity along the filament and across the strand;
- The heat capacity has to be averaged over the T_0-T_c temperature range;
- For Nb_3Sn, the heat capacity has to account for the presence of the bronze between the filaments, since the bronze induces proximity coupling (*i.e.* quantum-mechanical tunneling of Cooper pairs through the normal material between adjacent filaments).

Table 3.1 shows the maximum filament diameters calculated using relation 3.2 (where $d_{max} \approx 2a$) for a NbTi and an internal tin Nb_3Sn strand at 1T and 4.2K. The effective filament diameter of this latter strand was measured to be 116 μm, consistently with the hysteresis loop not showing any flux jump (see Section 7.3).

	NbTi @ 1T	Nb_3Sn @ 1T
J_c critical current density [A/m^2]	**6.0x10^9**	**1.1x10^{10}**
T_c critical temperature [K]	**8.6**	**17.8**
γ density [kg/m^3]	**6.2x10^3**	**8.6x10^3**
C specific heat [J/kg K]	**0.89**	**194**
d_{max} maximum stable diameter [μm]	**80.3**	**134.5**

Table 3.1 Maximum filament diameter to prevent flux jumps for NbTi and Nb_3Sn.

The second reason to require small filaments is to limit persistent magnetization currents in the superconductor (see Section 7.2), which are the sources of severe field distortions at low excitation of an accelerator magnet. These bipolar currents

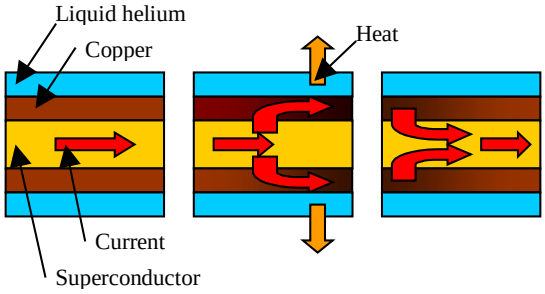

Figure 3.1 Cryogenic stabilization.

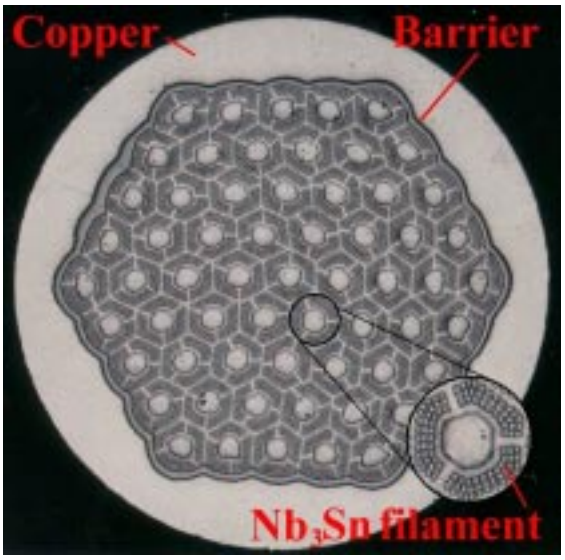

Figure 3.2 Nb_3Sn multifilamentary strand.

generate all the multipoles allowed by the coil symmetry. A distinct hysteresis behavior is also observed. Actually the restriction on filament diameter is more constraining for magnetization than for flux jumping. For NbTi, filament diameters of 5-6 μm are needed for relative deviations from ideal dipoles or quadrupoles on the order of 10^{-4}.

The filaments in a strand are also twisted with a pitch of 15-25 mm (more tightly than needed for stability against flux jumping) to suppress inter filament eddy currents induced during a field sweep across the matrix.

A high purity copper matrix is used to provide mechanical support and at the same time serves as an electrical bypass of high conductivity and as a heat sink. Figure 3.1 shows the general principle of the so-called cryogenic stabilization. If a filament should temporarily be heated beyond T_c, for instance due to a small flux jump, the current is taken over by the copper for a short moment. If the copper is sufficiently well cooled for the ohmic heating to be dissipated without excessive temperature rise, the superconductor eventually cools down and recovers superconductivity. Current transfers back to it from the copper and the ohmic heating ceases. To fulfill these tasks, the copper matrix must be in as good electrical and thermal contact with the superconductor as possible.

Figure 3.2 shows a typical cross section for an Intermagnetics General Corp. (IGC) intermediate tin Nb_3Sn strand with 61 split-subelements before thermal reaction. The non-copper region containing the split-subelements is

separated from the outer copper matrix by means of a tantalum barrier. Each subelement contains 106 Nb filaments.

To wind the magnet superconducting coils, the multifilamentary strands are bound together in a cable. The multi-strand cable is preferred to a single wire for the following reasons:

- It limits the length requirement for wire manufacturing. A coil wound with a cable having n strands requires piece lengths 1/n shorter with respect to a similar coil wound with a single wire;
- It allows strand to strand current redistribution in the case of localized defects or when a quench originates in one strand;
- It limits the number of turns and facilitates coil winding;
- It limits coil inductance.

The most commonly adopted cable is the so-called Rutherford type, in which the wires are twisted and compressed in two flat layers, as shown in Figure 3.3. For the High Field Magnet Project (HFM), Nb_3Sn cable samples have been produced at Lawrence Berkeley National Laboratory (LBNL) at Berkeley, CA, using 28 twisted strands with various packing factors. The packing factor is the ratio of the sum of the undeformed strand cross section areas with respect to the area of the enclosing trapezoid. Results of magnetization measurements of strands extracted from these cables will be presented in Section 7.5.

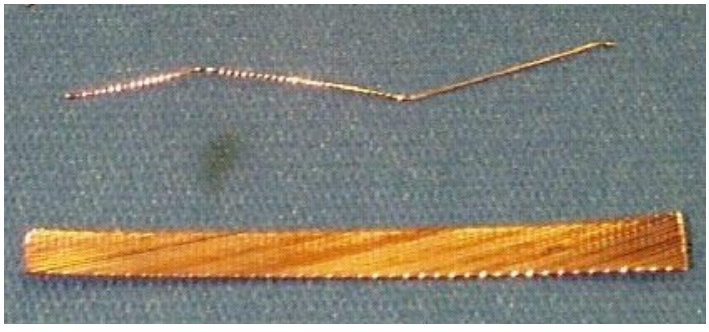

Figure 3.3 Superconducting Rutherford cable and extracted strand.

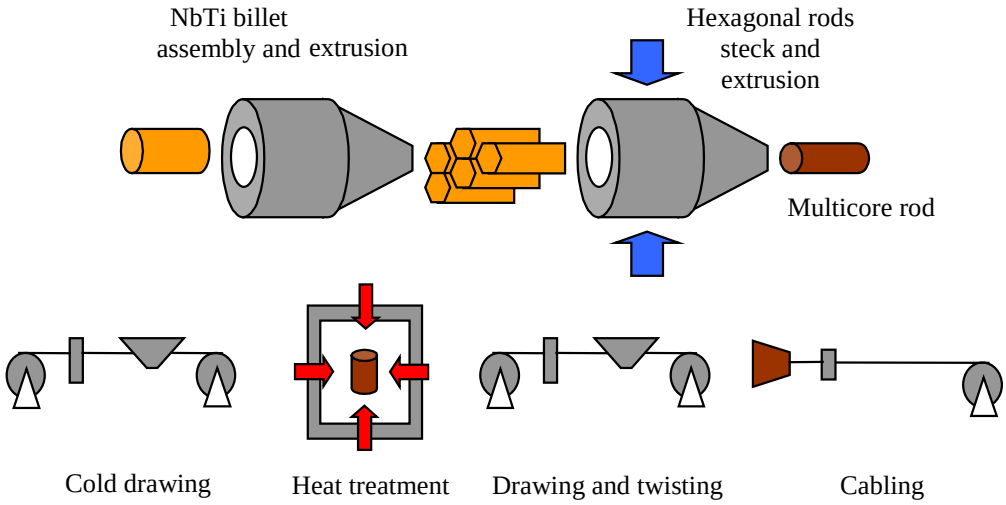

Figure 3.4 Production process for NbTi strand and cable.

3.3 NIOBIUM TITANIUM

Niobium and titanium are mutually soluble to form ductile alloys over a wide range of compositions. The critical properties vary with composition. Since optimum critical field and highest critical temperature do not occur at the same composition, commercial alloys are usually formulated for optimum critical field, in the range of Nb 46.5 to 50 wt% Ti. Otherwise a compromise must be found depending on the technological application of the strand. A ternary element, most commonly tantalum, may also be added to produce a modest increase in B_{c2} of 0.3 T at 4.2 K and 1.3 T at 1.8 K.

Originally it was thought that the principal source of flux pinning in the material came from the dislocation cell structure in the wire. It has now become clear that most of the pinning is provided by finely divided deposits of Ti α-phase. This is a hexagonal close packed titanium rich phase, which is precipitated on the dislocation cell boundaries as a result of the heat treatments applied during the manufacturing process. The α phase remains normally resistive at low temperature and has been shown to be a significant source of flux pinning sites.

Artificial pinning center (APC) techniques have been attempted in order to increase the field operating range and critical current. These techniques are based on the fine dispersion of second phase particles by mechanical processing. So far they have only allowed to achieve higher critical currents at low fields.

The request for higher field magnets has led to NbTi being used at temperatures lower than 4.2 K. This is the case of the Large Hadron Collider (LHC) at CERN. The magnets for this accelerator will work in superfluid helium (1.9K), where B_{c2} is increased from its 4.2 K value of 11 T to 14 T. The use of superfluid helium brings many other benefits in terms of better cooling and stability.

The manufacturing technology has been developed by different firms. Currently, the production of high J_c wires with filaments below 10 μm embedded in a high purity OFHC (Oxygen Free High Conductivity) copper matrix is normal practice. A scheme is shown in Figure 3.4. The first step of the process is to build a billet of high homogeneity NbTi alloy by arc vacuum melting. The NbTi is then fitted inside a copper extrusion can with a thin diffusion barrier of pure Nb interposed between the NbTi and the copper. The purpose of this barrier is to prevent the formation of $CuTi_2$ intermetallics during intermediate heat treatments, since they are hard and brittle, and break the filaments at the last stages of drawing. The billet is evacuated, electron-beam welded, and extruded. After cold drawing to size, the rod is drawn through a hexagonal die and then cut into many lengths. These lengths are stacked into another copper can, which is again sealed, extruded and drawn down to final size. For accelerator magnets, which may have up to 10^4 filaments, a double stack process is often used in which the rods are again drawn into hexagonal sections and stacked in another can. Multiple heat treatments are applied throughout the process in a defined sequence of alternating cold work and heat treatment, which has been found to produce the best configuration of α Ti precipitates and hence the best flux pinning. After reaching final size, the wire is twisted.

Typical properties of NbTi strand produced for LHC dipoles are listed in Table 3.2.

	IGC NbTi
Wire diameter [mm]	1.29
Filament diameter [μm]	5
Cu to non-Cu ratio	1.8
I_c at 8 T and 4.2K [A/mm^2]	1114

Table 3.2 NbTi properties for LHC.

3.4 NIOBIUM TIN

Nb_3Sn is an intermetallic compound having a well-defined stoichiometry and the A15 crystal structure. It shows higher critical temperature and field than NbTi. However, it is highly brittle after heat treatment, and extremely strain sensitive. Originally, because of this behavior, Nb_3Sn was produced in the form of tape, but it is not a useful shape for magnet design and new processing techniques had to be developed. In this compound, the dominant source of flux pinning appear to be the grain boundaries. In order to obtain high critical current densities is therefore necessary to produce a fine grain structure. This is in conflict with the long times necessary to diffuse the tin through the copper first and the niobium next, which make the grains grow. The optimum process is obtained by balancing these two issues and taking into accounting the material specific application.

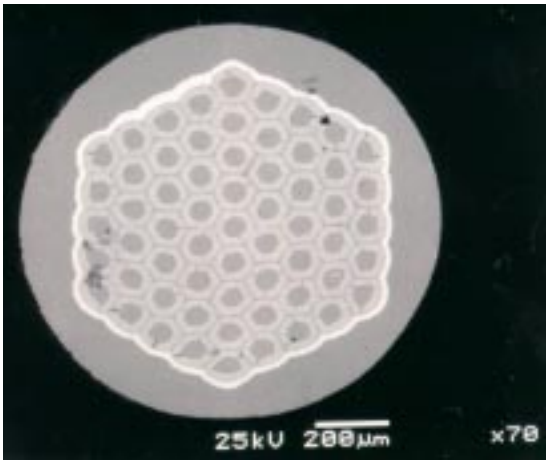

Figure 3.5 IGC Internal Tin Low Tin Nb_3Sn.

The critical current density, J_c, needs to be carefully defined. In NbTi one normally quotes the

critical current density in the superconductor, Jc_{NbTi}, and the critical current density on the whole strand cross section, J_{cav}. These two current densities are related to each other as follows:

$$J_{cav} = \lambda J_{cNbTi}, \tag{3.3}$$

where λ is the copper to superconductor ratio. For Nb_3Sn the distinction is complicated by the presence of the bronze between the filaments, generated from the diffusion of tin into the copper. Usually the critical current density is calculated in the non-copper part of the strand, which is comprehensive of both superconductor and bronze, while the overall average value, J_{cav}, is still calculated on the whole strand cross section.

Different manufacturing processes have been tested and developed in the last years by different companies. The most important ones are:

- Bronze process;
- Internal tin process (IT);
- Modified jelly roll process (MJR);
- Powder in tube process (PIT).

In these processes, the basic elements are shaped in the form of a composite strand. At this stage, the strand is still ductile and can be used to produce cables that are wound into magnets. The superconducting compound is formed after thermal reaction. This procedure is necessary because of the extreme brittleness and strain sensitivity of the final superconductor.

3.4.1 The bronze process

The bronze process is very similar to the fabrication of NbTi wires. A billet of ductile Nb rods, assembled in a bronze matrix, is extruded and drawn to the final size. The tin content in the bronze matrix being limited to less than 13.5wt% {limit for a ductile bronze alloy), a large bronze matrix is required to provide sufficient tin to the niobium rods. The initial billet is made of hundreds of Nb rods

and it is drawn into a hexagonal shaped element of intermediate size. The hexagonal rods are cut and reassembled in a second billet, which is extruded, annealed and drawn to the final wire size. Nb_3Sn wires are stabilized against flux jumping using OFHC copper. The copper has to be protected from the diffusion of the bronze-tin by a tantalum or niobium barrier. The niobium barrier is cheaper, but at low fields it is superconductive. This can cause field distortions, which can become intolerable in applications like particle accelerator magnets. In these cases a Tantalum barrier is preferred. The stabilizing copper can be incorporated internally with up to 27% of the wire cross section or externally with a copper part of 30-60%.

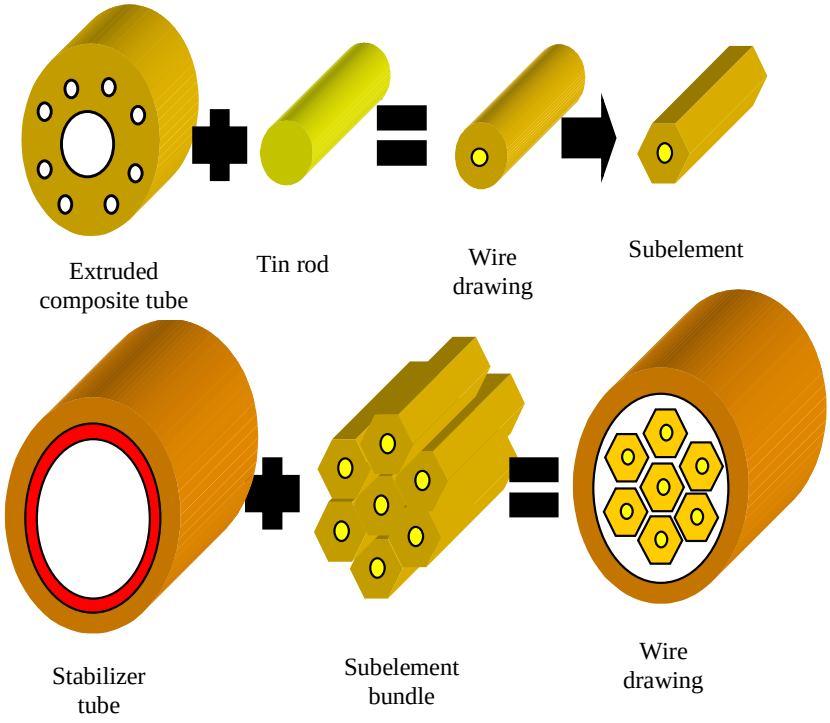

Figure 3.6 Internal Tin Process.

3.4.2 The internal tin process

The internal tin process was introduced to overcome the main limit of the bronze method, which is a limited tin content of 13.5wt% in the matrix. The idea was to distribute local tin sources surrounded by Nb rods and located in copper tubes. These tubes are drawn into hexagonal subelements, which are shortened

and reassembled into a new billet characterized by a stabilizing copper outer ring protected by a tantalum barrier. The billet is then drawn to the final wire size without intermediate annealing. Factors like the amount of tin (high, intermediate, and low content) and the subelement number characterize the conductor properties. Figure 3.5 shows a reacted Nb_3Sn conductor of 1mm in diameter by IGC, having a low tin content and 61 subelements.

3.4.3 The modified jelly roll

The modified jelly roll is a variant of the internal tin method pursued by Teledyne Wah Chang company in the US. It consists of two parallel sheets of niobium and copper rolled around a solid tin rod. In this way the niobium part in the non-copper area is increased to 35%. The roll is inserted in a copper tube to form a billet. During drawing the niobium cross section is reduced by ~750 times and shaped as a hexagonal rod. A second billet is then assembled using the hexagonal rods, and drawn to the final wire size. No annealing is required during the process. Protecting barriers have to be inserted between the tin core and the niobium sheet, between the niobium and copper sheets, and before the external stabilizing copper. For this purpose tantalum, vanadium, and niobium are used. Figure 3.7 illustrates the main steps of this process.

Figure 3.7 Modified jelly roll.

3.4.4 The powder in tube process

The powder in tube process was first developed by the Netherlands Research Foundation and is presently adopted by the Shape Metal Innovation Company [21]. The basic idea is to fill hollow Nb tubes with fine granulated Nb_2Sn powder and then place them into a Cu matrix. Compared to other methods, a large portion of the non-active bronze content can be replaced by

superconductor elements or stabilizing Cu. The non-reacted part of the outer Nb tube acts as barrier between Cu and Nb_3Sn. The recent development of this technique has allowed producing long 36 and 192 filament strands. In laboratory, samples of 1332 filament strands were also obtained [22]. The next step for large scale PIT strand will be the realization of a 492 filament strand with an effective filament diameter of about only 20 μm.

3.5 SUMMARY

The properties of superconductors and their manufacturing process have been briefly described in this chapter. At the Technical Division of Fermilab, an apparatus has been setup in order to measure magnetization properties of Nb_3Sn multifilamentary strands. The setup sensitivity was tuned to the expected magnetization signal in this material. NbTi strands were also measured. This setup is described in the next chapter. The measurements made are the original work performed for this thesis.

CHAPTER

4

EXPERIMENTAL SETUP

4.1 INTRODUCTION

Measurement techniques for the magnetic properties of superconductors do not differ in principle from those used for normal metals. However, they must be suitable for use at very low temperatures. The experimental setup includes cryogenic devices and a superconducting solenoid to provide an external magnetic field.

4.2 MEASUREMENT TECHNIQUES

Several methods are used to perform magnetization measurements of superconducting strands. The most common are:

- Vibrating Sample Magnetometer;
- Hall probe;
- SQUID magnetometer;
- Balanced coil magnetometer.

The method chosen in the present work is the balanced coil magnetometer, which is thoroughly described in the next sections. In this section the three other methods are briefly described.

4.2.1 Vibrating Sample Magnetometer (VSM)

In this setup, the specimen is moved in and out of two pick up coils connected to a ballistic galvanometer. The amplitude of the galvanometer signal is proportional to the flux in the sample, *i.e.* to its magnetization. The method is illustrated in Figure 4.1. The sample is mounted at the end of a rod connected to a mechanical resonator, which makes it oscillate at a fixed frequency through two pick up coils A and B. These almost identical coils are connected in series with opposite polarity. A steady external magnetic field of the appropriate magnitude is supplied by means of solenoid S.

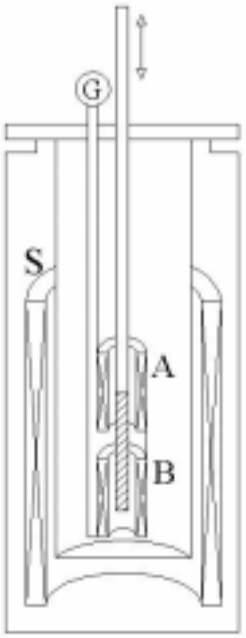

Figure 4.1 Scheme of the vibrating sample method.

In the case of a diamagnetic sample, if the sample is moved from coil A to coil B, the flux threading coil A will increase and the one in B decrease. Since the two coils are connected in series opposition, the induced EMFs get subtracted and the ballistic galvanometer, or a lock-in amplifier, will swing by an amount proportional to the magnetization of the sample.

The steady external field is increased in steps after each measurement, allowing to measure the hysteresis curve of the material.

4.2.2 Hall probe

In this setup, magnetization is measured by a micro hall probe in the vicinity of a straight piece of wire. The sample is placed in a magnetic field generated by a solenoidal magnet, which is ramped with low field sweep (10 mT/s) to eliminate the effect of eddy currents. The probe is mounted on the wire

at a known distance from its axis. The active area of the Hall crystal is exposed to all magnetic effects present in the system, including the applied external field, the sample magnetization, and residual magnet magnetization. A resistor connected in series with the magnet can compensate the external field, which is proportional to the current in the magnet. Therefore, after placing the sample, the signal measured is the sum of sample and magnet magnetizations. Without sample, the signal measured is the hysteresis loop of the magnet magnetization.

By subtracting the two signals, one finds the hysteresis curve of the specimen. Better results can be obtained using a second Hall probe exposed only to the external field, in order to compensate the magnet hysteresis by taking the difference of the probe outputs. In this case, two probes with the same characteristics are used [23].

4.2.3 SQUID magnetometer

In a Superconducting Quantum Interference Device (SQUID) magnetometer, as for the other techniques, the magnetic field is provided by a superconducting magnet. The sample is surrounded by a superconducting sensing coils, which are coupled through superconducting circuitry to a SQUID device. The magnetization of the sample changes the magnetic flux through the sensing coil, inducing a supercurrent, which changes the flux in the SQUID and produces a change in its output signal. This device is similar to the VSM, but works in DC mode, with the SQUID device operating as a very low noise amplifier.

All these interesting methods feature advantages as well disadvantages.
The VSM is straightforward and the electronics cost is low, but the sample movement can produce some noise, due to vibration transmission. Only small samples can be tested, which worsens the accuracy. Moreover measurements are performed at constant field and, since for an accurate hysteresis curve many points have to be acquired, the measurement can be very long.

In the Hall probe technique, accuracy is also compromised by a small specimen.

The extremely high sensitivity of the SQUID magnetometer leads to some technical difficulties. A SQUID not only does detect the drift due to *flux creep* in the superconducting magnet and to relaxation of mechanical stress in the solenoid windings, but it is also sensitive to magnetization changes of the structural materials near the sensing coils, so that it is necessary to perform a measurement without the sample in order to zero the device. These problems and the fact that data cannot be recorded continuously, as the external field is swept in steps, make this technique extremely expensive and difficult to apply.

Within the existent Short Sample Test Facility (SSTF), comprising a 15/17 T magneto-cryostat, the balanced coil magnetometer was chosen to perform the magnetization measurements reported in this thesis.

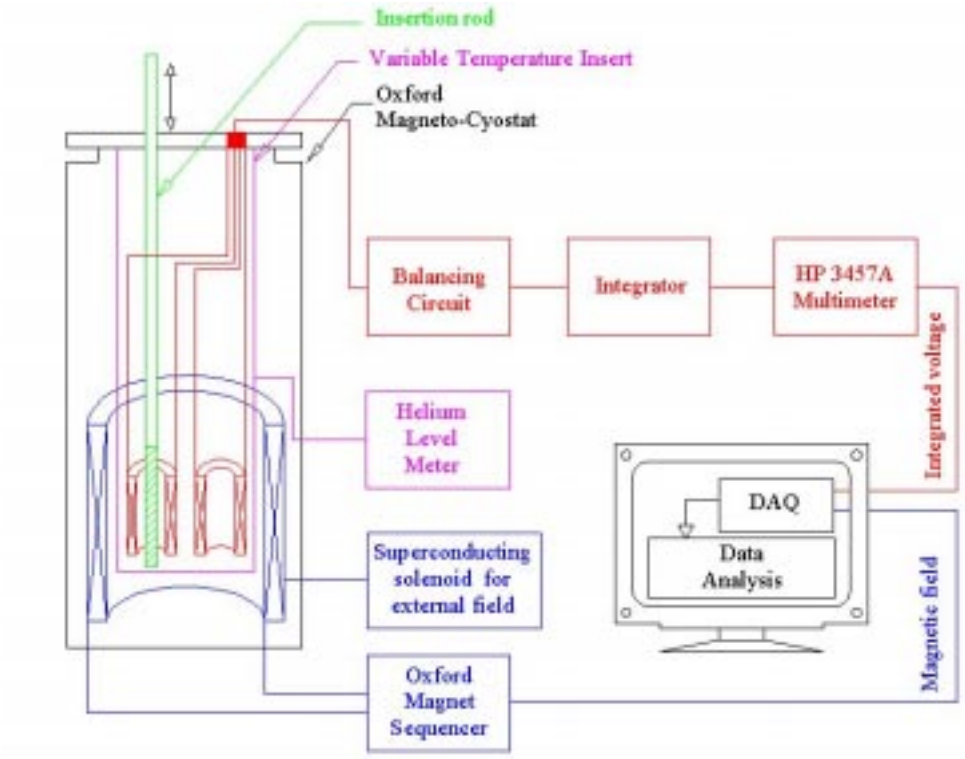

Figure 4.2 Balanced coil magnetometer.

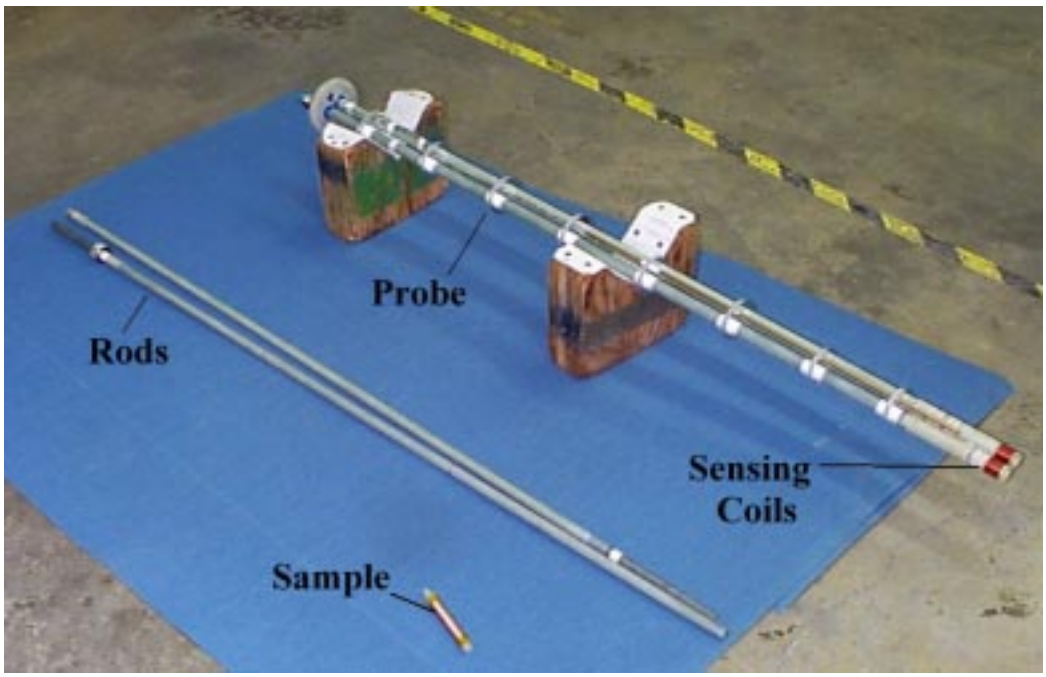

Figure 4.3 Setup.

4.3 BALANCED COIL MAGNETOMETER

The technique chosen here is the balanced coil magnetometer [24]. The experiment operates at boiling helium temperature of 4.2 K. A vapor-cooled magneto-cryostat equipped with a superconducting solenoid is used. The magnet is ramped to create an external varying magnetic field, which induces an EMF in two almost identical coils (balancing and pick up) connected in series with opposite polarity to provide an almost zero signal. An experimental scheme is shown in Figure 4.2 [25]. When a sample is placed in the pick up coil, a perturbation in the magnetic field is generated due to the magnetization of the superconducting specimen.

The measurement is divided in two steps. First, a magnetic cycle is performed without sample in order to acquire the EMF generated in the sensing coils, which is a measure of the background (*BKG*). Next, an identical cycle is run

Figure 4.4 Sensing coils.

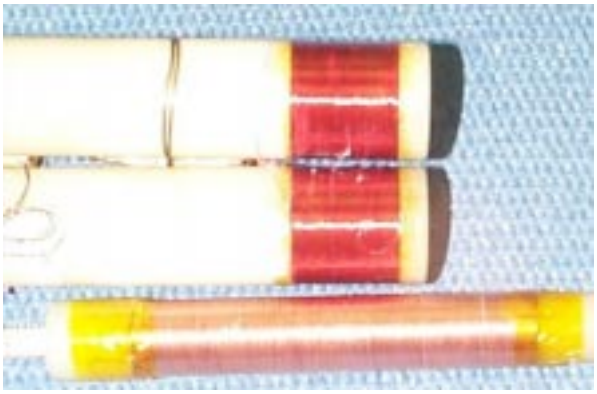

Figure 4.5 Sensing coils and sample.

with the sample inserted in the pick up coil. In this case the induced EMF includes background and signal (*SIGNAL*). By subtracting the two measurements, one obtains the magnetization of the superconducting sample.

The signal from the coils is sent to a balancing circuit and is then integrated. As shown in Figure 4.3, the two coils are supported at the bottom of a G10 probe, which is used to reach the measurement zone within the cryostat, approximately at the center of the solenoid. A close-up view of the coils is shown in Figure 4.4, and their geometry is specified in Table 4.1:

	Pick up coil	Balancing coil
Diameter [mm]	**~22.20**	**~22.20**
Winding [turns]	**597**	**597**
Resistance @ 300 K [Ω]	**46.48**	**45.85**
Resistance @ 4.2 K [Ω]	**1.60**	**1.57**

Table 4.1 Pick up and balancing coils geometry.

As shown in Figure 4.5 the sample is a coil tightly wound on a G10 holder. The G10 holder is fixed at the bottom of a rod in order to center the sample within the pick up coil. This procedure allows one to measure different samples without warming up the whole cryostat.

4.4 THE MAGNETO-CRYOSTAT

The magneto-cryostat is an Oxford Instruments Teslatron, shown in Figure 4.6 [26]. Detailed specifications are given in Appendix A. It consists primarily of a large helium dewar (Main Bath) containing a superconducting solenoid at the bottom. To allow measuring at different temperatures, the main cryostat feeds a second smaller helium cryostat, called Variable Temperature Insert (VTI), which is inserted inside the main dewar, down into the solenoid bore. According to Oxford specifications, the VTI allows a temperature range between 1.5 K and 200 K.

The cooling process of the device lasts about two days. The VTI and the Main Bath are first pumped and flushed with helium gas. Then liquid nitrogen is used overnight to precool the Main Bath at 77 K. Next, the pumping and flushing phase with helium gas is repeated to ensure that no liquid nitrogen is left. Finally, the dewar is filled with liquid helium to reach 4.2 K, *i.e.* the equilibrium temperature of the system thanks to natural evaporation of helium. The coolant is driven in the VTI through a needle valve, by means of a pressure gradient between the two vessels. During measurements, because of the Joule effect in resistive elements, the helium in the VTI boils off and is vented out trough piping. When the Main Bath has lost all its reserve of liquid helium, due to heat leak and Joule effect, it can be refilled directly with liquid helium only if the

Figure 4.6 Teslatron and piping.

temperature of the superconducting magnet is still below boiling nitrogen. If this temperature is over 77 K, the cool down procedure has to be repeated. Usually, if the VTI is kept filled of helium, and no probe is present, the helium reserve in the Main Bath can last up to 3 days.

To operate at temperatures higher or lower than 4.2 K, a proportional, integral, derivative (PID) control is used. An Oxford software controls a heater placed at the bottom of the VTI that can be operated too increase the temperature, and regulates the aperture of the needle valve located between the Main Bath and the VTI to increase coolant flow. This temperature control system is made more effective by connecting the VTI to a vacuum system. In this way, the convection of the coolant is forced and a better heat exchange is obtained with respect to natural convection. The vacuum system includes two pumps is series, a roots blower and a rotary rougher. The blower applies a 80 mbar pressure gradient with a 1500 l/s nominal pumping speed and is provided with a 4 kW motor, while the rougher applies a 4 mbar pressure with a 420 l/s nominal pumping speed and is provided with a 8.8 kW motor.

The temperature in the VTI is monitored by a Cernox, which is a resistive sensor suitable for operating at low temperatures with good sensitivity and not affected by the presence of magnetic fields up to 20 Tesla. A Cernox is also used to measure the magnet temperature. The helium level in the Main Bath is measured by a sensor consisting of a superconducting wire that extends from the top to the bottom of the dewar. The portion of wire below the liquid surface at 4.2 K shows a superconducting behavior, whereas a small heater on the wire ensures that the upper part be kept above its critical temperature. A current is made to flow in the wire at some fixed intervals, and the helium level is derived by measuring the voltage between the wire extremities. The helium level in the Main Bath is measured every few minutes. The VTI helium level is measured every few seconds by placing the superconducting sensor on the probe used for the magnetization measurements.

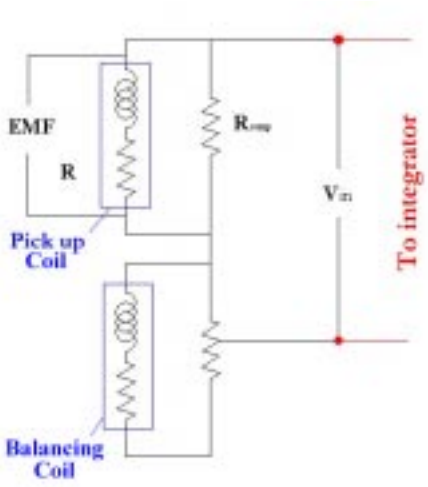

Figure 4.7 Balancing circuit.

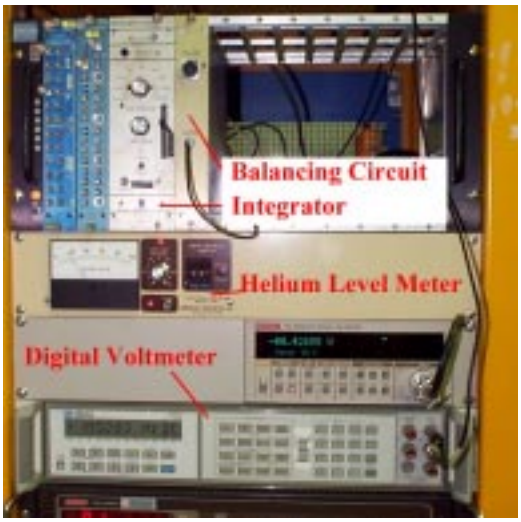

Figure 4.8 Electronics.

4.5 THE ELECTRONICS

The electronics for these magnetization measurements is fully integrated with a PC system in order to easily record, analyze and store data. The signal coming from the pickup and balancing coils is sent sequentially to a balancing circuit, an integrator and a digital voltmeter so as to be acquired by the PC through a General Purpose Interface Bus (GPIB) card. These instruments are shown in Figure 4.8.

The balancing circuit is necessary to correct the difference between the two sensing coils. Although they must be similar a slight difference in resistivity is to be expected. The balancing circuit, shown in Figure 4.7, consists of two resistors connected in parallel with the two coils. The resistor on the pickup coil, R_{comp}, is constant while the one on the balancing coil is a potentiometer, which allows to adjust to zero the output when no sample is present in the device. The signal coming from the balancing circuit is then sent to a NIM integrator. This electronic device integrates the signal with low drift. Usually the time constant is set at 100ms. A Hewlett Packard 3547A digital multimeter equipped with a GPIB

standard output was used to send data from the integrator to the PC. The GPIB, or ANSI/IEEE Standard 488.2, is a digital, 8-bit parallel communication interface with a data transfer rate of 1 Mbytes/s, using a three-wire handshake. It allows connecting to the same bus up to 14 instruments, and sending and receiving data trough different devices at the same time.

The magnet is controlled by an Oxford Intelligent Magnet Power Supply (IPS 120-10) with a GPIB output. It is specifically built to energize and control a wide range of superconducting magnets. It provides a bipolar current and allows the magnetic field to be swept smoothly through zero in either direction. The ramp rate sequence can be programmed trough an application software and customized by the operator.

The only instrument that is not connected to a computer is the helium level meter. It is an American Magnetics Liquid helium Level meter model 130A equipped with a single channel input. In practice, during the measurements the liquid level does not varying very much.

All data are transferred to an Intel Pentium II based PC with 128 Mbytes RAM, operating under MS Window NT4 platform, trough an AT-GPIB TNT (PnP) card.

4.6 DATA ACQUISITION AND ANALYSIS SOFTWARE

The evolution of fast and powerful computers in the last 20 years has allowed the development of friendly program languages for interfacing to a variety of instruments. Computerized control is needed not only for automation, but also to integrate the data acquisition (DAQ) with data analysis and storage. One of the most used programming languages is National Instruments LabView. It is a graphical language (G language) that can be interfaced to C or C++ routines. Almost all new instruments are provided with "drivers" and specific "functions" for an easy implementation in LabView. The most powerful feature of this language is that it is based on a graphical user friendly structure. The IEEE

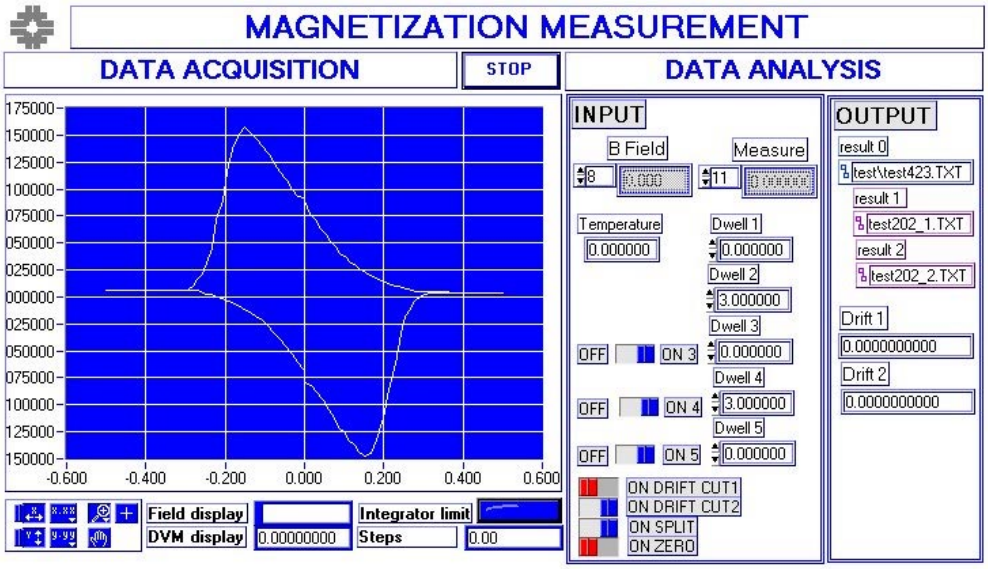

Figure 4.9 Data acquisition GUI.

488 standard can be implemented also trough a C or C++ program, but the interface with the instrument is not easy to apply and construct. When an error in sending a command string to the instrument occurs, it is not easy to find out the solution of the problem. In LabView, trough the VISA tracking system, the first error occurring during the execution of the application is recorded in an output error log file, and the correction procedure is simplified. Usually a "front panel" (VI or "virtual instrument") of the device is reproduced on the screen and the instrument can be piloted trough the PC instead of working on the physical buttons and display. Moreover data can be manipulated and stored automatically after the measurements.

The magneto-cryostat is provided with fully automated LabView software. The needle valve and the heater in the VTI are monitored and managed trough Oxford software. To ramp the magnet and generate a cycle for the magnetization measurements, Oxford IPS application, whose front panel is shown in Figure 4.10, is used. For data acquisition and analysis, a LabView application had to be written. This was a qualitatively significant component of this thesis. Its front panel, shown in Figure 4.9, displays the construction of the hystesis curve on line, while data are acquired and stored in an ASCII file. This code can be divided in

two phases, data acquisition and data analysis. The first phase talks to the multimeter and to Oxford IPS to acquire data during the ramping of the magnet. The second phase takes over when the measurement is completed: the drift of the integrator is automatically cut, the output file is split if more than one magnetic field cycle per measurement is performed, and the initial offset of the curve is set to zero. The measurement is customizable by the operator, and any operation can be enabled or disabled in order to perform different cycles.

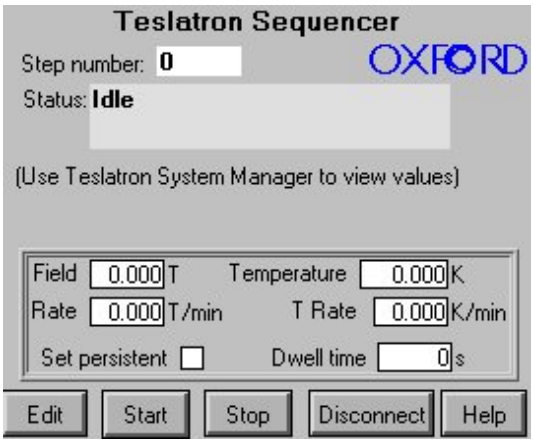

Figure 4.10 Oxford IPS software.

In order to be able to subtract the background from the sample measurement, the former was interpolated to obtain a continuous function of magnetic field. A LabView VI was created to perform this operation as the most efficient way to automate the process.

4.7 SAMPLE PREPARATION

The preparation of the sample includes a number of steps that are different in the case of Nb_3Sn with respect to NbTi, since the latter does not need heat treatment. The procedure for Nb_3Sn is described here. For NbTi, the same steps except those related to reaction preparation have to be applied.

The sample is first shaped like a coil, by winding it on a rod that has a diameter a few millimeters smaller than the sample holder, to take into account the elastic spring-back of the material. During heat treatment, a stainless steel tube is used to hold the specimen. The tube is first sprayed with a graphite lubricant to prevent its sintering to the sample during the reaction. The sample, as shown in Figure 4.11, is tightly wound on the tube, tied with stainless steel wire, and

Figure 4.11 Sample preparation.

washers are used to carve identification labels on them. Some strand is left free at the specimen ends to account for tin leakage during heat treatment.

After reaction the specimen tails are cut, and the sample is slid out of the tube and slipped on a G10 holder. The procedure of changing holders is very delicate because reacted Nb_3Sn is brittle. Although a magnetization measurement is not very strain sensitive (see Chapter 7), results between an unstrained and a strained specimen can nevertheless differ by a few percents.

G10 is a glass-fiber epoxy, hence a non-magnetic material, as required for magnetization measurements to best reduce noise. At first, the same stainless steel tube used for reaction was used for the measurement, but it was found that using a G10 holder reduced the error by an order of magnitude.

The sample is blocked on the G10 holder by means of acrylic adhesive at the edges. During sample preparation, all dimensions are checked. Specifically, the length of the coil, the number of turns, and the strand diameter have to be carefully measured in order to calculate magnetization. Table 4.2 shows the average dimensions of the sample:

	Sample
Strand diameter [mm]	**~1.00**
Holder diameter [mm]	**13.20**
Winding [turns]	**75**
Coil height [mm]	**75.00**
Cross section [mm^2]	**25.00**

Table 4.2 Sample geometry.

For NbTi specimens, after winding the coil shaped sample is directly slipped, and its ends fixed on the G10 holder. Because of the smaller signal of NbTi with respect to Nb_3Sn, a double layer sample is usually adopted. Kapton tape insulator is wound in between the two coil layers to avoid current flow across layers. This procedure doubles the cross section area of the material transverse to the external magnetic flux, thus doubling the signal.

CHAPTER

5

THEORY OF MAGNETIZATION MEASUREMENTS

5.1 INTRODUCTION

The experimental data obtained as described in Chapter 4 are proportional to the sample magnetization and can be directly used for relative comparisons. However, to obtain the correct magnetization value, some geometrical factors have to be applied to the raw output voltage from the integrator. In addition, some corrections for systematic effects have to be applied.

5.2 THE BALANCED COIL MAGNETOMETER

The balanced coil magnetometer is based on the Lenz principle. A time varying magnetic field induces an EMF in a conductor. As shown in Chapter 4, two sensing coils connected in opposite series are placed in a varying magnetic field, B_0. One of the coils contains the superconducting sample, whose magnetization will induce an EMF in it.

To find the hysteresis curve of the specimen, two measurements are performed. The first one is done with no sample to find the background (*BKG*). In

this case, the following expression can be written for the EMF generated in the coils:

$$BKG = N_p S_p \frac{dB_0}{dt} - gN_b S_b \frac{dB_0}{dt}, \tag{5.1}$$

where:

N_p is the number of turns of the pick up coil,
S_p is the area within the pick up coil [m^2],
N_b is the number of turns of the balancing coil,
S_b is the area within the balancing coil [m^2], and
g is the balancing factor.

The second measurement is done with the sample in the pick up coil. In this latter case, the induced EMF, including the *BKG* and the superconductive signal (*SIGNAL*) can be written as follows:

$$TOTAL = N_p S_p \frac{dB_0}{dt} - gN_b S_b \frac{dB_0}{dt} - N_p S \frac{dM}{dt}, \tag{5.2}$$

where:

S is the cross section of the sample [m^2], and
M is the sample magnetization [T].

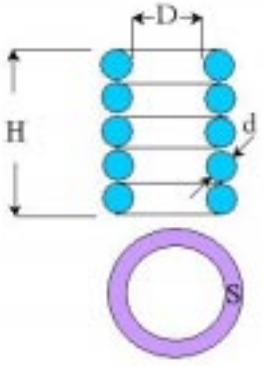

Figure 5.1 Sample cross section.

The cross section of the sample is computed from its geometry, shown in Figure 5.1, as follows:

$$S = \frac{\pi^2}{4} d^2 \frac{T}{H} \sqrt{(D+d)^2 + \frac{d^2}{4}}, \tag{5.3}$$

where d is the measured strand diameter, D is the holder external diameter, T is the number of turns, and H is the coil height. Alternatively, by

knowing the sample weight and density, it is possible to infer *S* without having to introduce any measurement error on the specimen and holder diameters.

By subtracting the two measurements, one obtains the signal from the superconducting strand:

$$SIGNAL = TOTAL - BKG = -N_p S \frac{dM}{dt}. \tag{5.4}$$

The balancing circuit provides the EMF signal modulo a scaling factor, since the measured quantity is V_{in} , as shown in Figure 5.2. This factor can be evaluated as:

$$\frac{EMF}{V_{in}} = (1 + R/R_{comp}). \tag{5.5}$$

The resistance at 4.2 K of the two sensing coils is very small. While at room temperature the resistance of the pick up coil and of the balancing coil is 46.48 Ω and 45.85 Ω respectively, at 4.2 K these values drop respectively to 1.60 Ω and 1.57 Ω. Since in the balancing circuit a 2 kΩ resistor, R_{comp}, is used, the corrective factor is 1.0008, which can be taken as 1 within the accuracy of the present measurement.

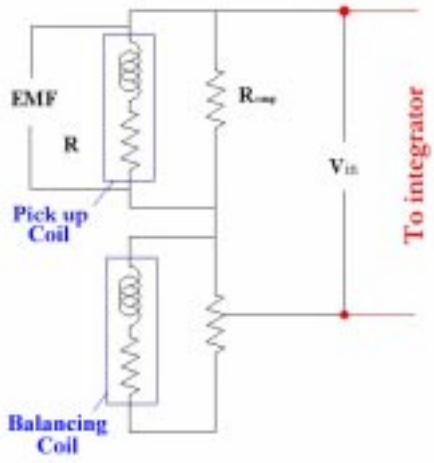

Figure 5.2 Balancing circuit effect.

The signal is then integrated by the integrator, V_{out}, as follows:

$$V_{out} = \frac{1}{\tau}\int V_{in}\ dt, \tag{5.6}$$

where τ is the time constant of the integrator (100 ms).

By taking into account the balancing circuit effect and the integration, equation (5.4) becomes:

$$M = -\frac{\tau}{N_p S}\left(1+\frac{R}{R_{comp}}\right)V_{out} \ . \tag{5.7}$$

5.3 EDDY CURRENTS EFFECT

A varying magnetic field induces currents in all exposed conducting materials. For NbTi and Nb_3Sn multifilamentary composites, coupling currents arise between different filaments through the resistive matrix (copper or bronze respectively). An effective method to reduce this effect is to twist the wire. Thereby the length of the loop exposed to the time-varying magnetic field is shortened and the contributions from adjacent loops alternate in sign. The eddy currents contribution to a magnetization measurement depends on the ramp rate of the external magnetic field:

$$M = M_{hyst}(B) + M_{eddy}(\dot{B}). \tag{5.8}$$

This effect was measured experimentally by repeating the same cycle from zero to 2 T using different magnet ramp rates (1.5, 1, 0.75, and 0.5 T/min). The AC losses and the magnetization at 1.2 T were then linearly extrapolated to a zero ramp rate.

This analysis was first performed for samples mounted on stainless steel tubes, as described in Chapter 4. The results for the magnetization at 1.2 T are shown in Figure 5.3. For a ramp rate of 1 T/min, the eddy current effect was about 30%. By repeating the same experiment using G10 holders, approximately zero effect was observed, as also shown in Figure 5.3 (red plot). More precisely, this effect produced data, at different ramp rate, with a standard deviation of 4 mT (1%), which is comparable with the measurement uncertainty of 2 mT (0.5%).

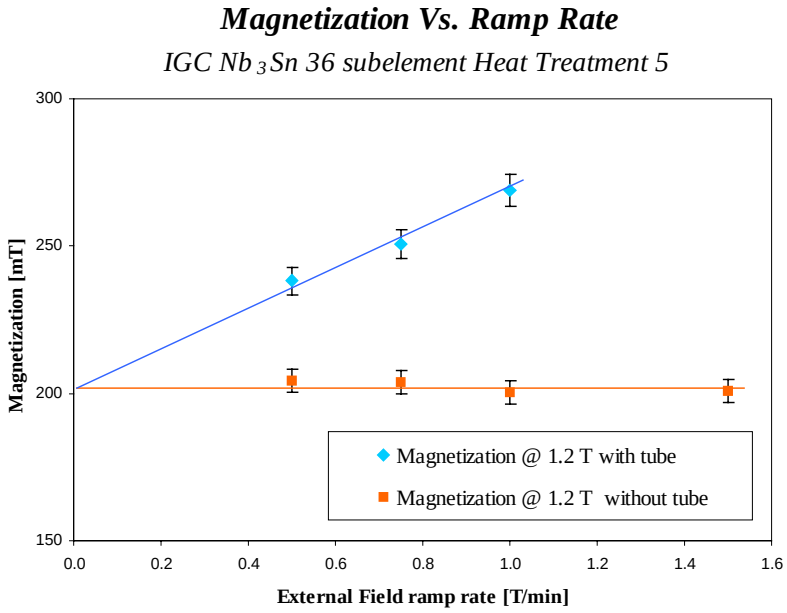

Figure 5.3 Eddy currents effect on magnetization at low field.

The difference between the two results is due to the presence of the stainless steel tube, which creates a coupling between the strands and allows the currents to flow all over the sample.

An analytical solution of the problem was also investigated, following the model given by Morgan in 1970, specifically formulated for multifilamentary twisted composites [18]. According to this theory, magnetization due to eddy currents in a strand is:

$$M_{eddy} = \frac{1}{\rho_{et}} \left(\frac{L}{2\pi} \right)^2 \dot{B}, \tag{5.9}$$

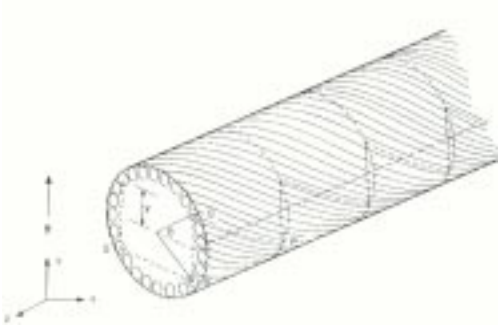

Figure 5.4 Multifilamentary strand.

where L is the twist pitch length of the strand, and ρ_{et} is the effective transverse resistivity of the material. The strand tested here had a 15 mm twist pitch and an effective transverse resistivity of $2 \cdot 10^{-8}$ Ωm. The calculated effect of the eddy currents

with a magnet ramp rate of 1 T/min (usually adopted during measurements) is about 0.060 mT. This gives a contribution of only about 0.03% the overall magnetization at 1.2 T.

Since this effect does not depend on the value of the field, but only on its variation, it should be stronger at high fields where magnetization is smaller. At 12 T, a contribution of 0.4% was evaluated. To confirm this expectation, the experiment at different ramp rates was repeated with cycles around 12 T. Figure 5.5 shows the ramp rate dependence of magnetization for a sample mounted on a G10 holder. As can be seen, the effect of eddy currents is not detectable at 12 T, where the accuracy of the measurement is 0.45%.

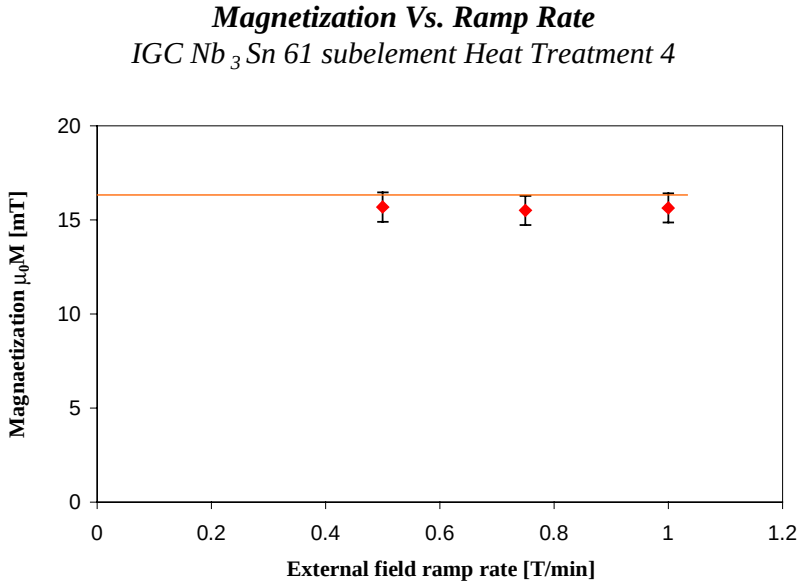

Figure 5.5 Eddy currents effect on magnetization at high field without stainless steel tube.

For measurements using stainless steel tubes, correction factors were applied according to the above results to both AC losses and magnetization computations.

5.4 SAMPLE MAGNETIZATION EFFECT

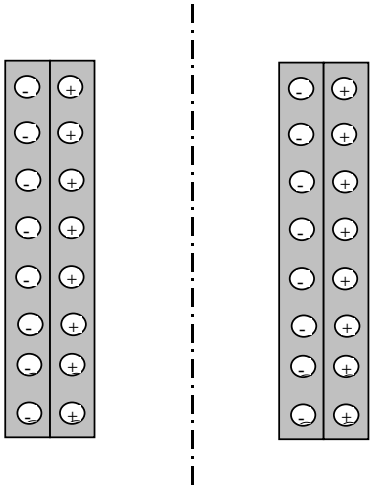

Figure 5.6 Finite element model.

The equations developed in this chapter are correct for an ideal sample of infinite length. In this case, the effect of autoinduction, due to the supercurrents generated by the magnetization of the superconducting material, is zero. In practice, the shorter the sample, the stronger is this effect.

A finite element model was used to understand how much this effect contributes to the final results of the measurements. This analysis was performed with OPERA, a specialized software in electromagnetic design from Vector Fields Ltd.. Since the problem presents an axial symmetry in both the geometry and the magnetic field, it was solved through a 2D model. The solenoidal sample is modeled by a tube of cylindrical shape with the same volume, average diameter, and height. The current flowing in the sample is only that related to its magnetization, due to its open shape. As shown in Figure 5.6, its rectangular section can be divided in two parts, inside which the magnetization current flows in opposite directions creating a closed circuit. This current configuration creates a magnetic field opposite to the external field. Its effect is to decrease the signal acquired trough the sensing coils, with respect to the real magnetization of the sample. If a is the width and l is the height of the rectangular shaped section, and J is the current density, the magnetization of the material is equal to:

$$M = J\frac{a}{2}. \tag{5.10}$$

The equivalent current can be calculated as:

$$I = Ml. \tag{5.11}$$

The field distribution due to this current circulation is shown in Figure 5.7.

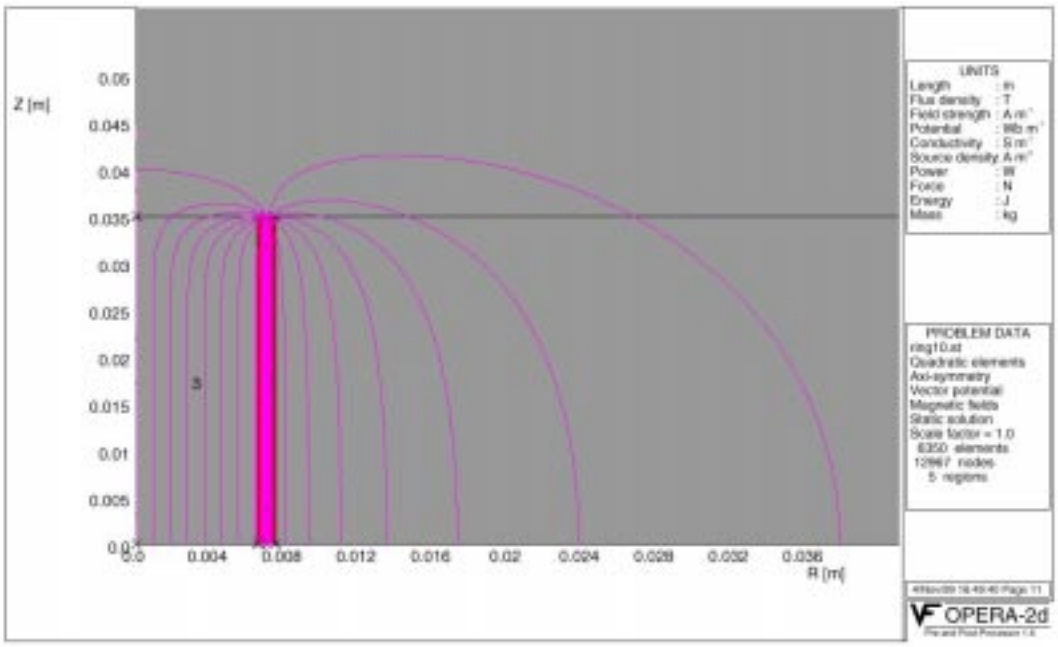

Figure 5.7 Finite element result.

To correct the self-induction effect, the total magnetic field generated by the sample and acquired by the pick up coil has to be taken into account. This effect can be added to equation 5.4 as:

$$SIGNAL = -N_p\left(S\frac{dM}{dt} - \frac{d\phi_{mag}}{dt}\right), \tag{5.12}$$

where ϕ_{mag} is the magnetic flux generated by the sample magnetization. Dividing and multipling the self-induction term for the magnetization, *M*, and the sample equivalent area perpendicular to the flux, *S*, after integration one obtains:

$$\int SIGNALdt = -N_p S(1-k)M\,, \tag{5.13}$$

where k is equal to:

$$k = \frac{\phi_{mag}}{MS}. \tag{5.14}$$

The value of this paramenter, calculated through the finite element analysis is very small, and the auto-induction effect can be considered negligible. The final equation for magnetization becomes:

$$M = -\frac{\tau}{N_p S}\left(1 + \frac{R}{R_{comp}}\right)\left(\frac{1}{1-k}\right)V_{out}. \tag{5.15}$$

5.5 SUMMARY

In this section, the correct scale factor between the experimental signal and true magnetization was computed. It was shown that phenomena like eddy currents and self-induction in the sample are negligible. Also electronic elements like the balancing circuit barely modify the signal. Only the geometrical parameters are responsible for scaling the signal to the absolute magnetization value. This conclusion was confirmed by the calibration of the device, described in the next section.

CHAPTER

6

ERROR ANALYSIS AND CALIBRATION

6.1 INTRODUCTION

Magnetization measurements are sensitive to the geometrical dimensions of the sample, which have to be accurately measured, and to the integrator drift. A theoretical error analysis was performed, and then checked using the self-calibrating feature of superconductors. For an absolute calibration of the system, the reversible magnetization of Nb alloys during the Meissner state was used.

6.2 ERROR ANALYSIS

As seen from equation 5.15, reported here for convenience:

$$M = -\frac{\tau}{N_p S}\left(1+\frac{R}{R_{comp}}\right)\left(\frac{1}{1-k}\right)V_{out}, \qquad (6.1)$$

the magnetization of a superconducting sample depends on many factors. The most relevant error sources are the measurement uncertainty of the sample area, S, and of the integrated signal, V_{out}. As an estimate of the overall measurement error,

the errors associated to these two parameters were evaluated separately, and then combined through error propagation.

To control geometrical errors, the diameter of the strand, the diameter of the holder, and the height of the sample have to be accurately measured. To achieve a precision of 0.001 mm, a Mitutoyo digital micrometer was used. Nevertheless, the uncertainty on the strand diameter is larger due to the sample shape, *i.e.* a coil of about 13 mm in diameter. The diameter has to be measured after the thermal reaction because during heat treatment dimensions change, due to the formation of superconducting A15 phase.

The error analysis was performed on a Nb_3Sn strand that showed the largest errors.

The strand nominal diameter was 1 mm before heat treatments, while after the reaction it showed the following average and rms values:

$$1.0227 \text{ mm} \pm 0.0037$$

where the rms corresponds to an error of 0.36%. The sample holder used in the experiments is always the same and has been measured many times obtaining:

$$13.2000 \text{ mm} \pm 0.0860$$

where the rms corresponds to an error of 0.65%. The height of the sample was measured with a larger Mitutoyo micrometer able to reach 200 mm with a precision of 0.01 mm. This dimension varies from sample to sample. The one used for this analysis was:

$$71.28 \text{ mm} \pm 0.10$$

where the rms corresponds to an error of 0.14%. Error propagation of these errors affects the calculation of *S*, as given by equation (5.3), by an error of 1%.

The measurement uncertainty of the integrated signal is affected by the presence of the background that has to be subtracted from the magnetization

signal, as shown in equation 5.4. The error associated to this subtraction is relevantly larger at high fields where the magnetization signal is lower, whereas the background is about the same. The difference in error between the AC losses and the magnetization measurements is related to magnetization being a point measurement (*i.e.* at a given field), while the AC losses being the total area of the hysteresis loop, measurement fluctuations cancel. Table 6.1 shows the error analysis at low and high field.

	V_{out} uncertainty	S uncertainty	Total error %
AC Losses 0-3 T	**0.37**	**1**	**1.1**
AC Losses 10-13 T	**1.72**	**1**	**2.0**
Magnetization @ 1.2 T	**0.45**	**1**	**1.1**
Magnetization @ 12 T	**3.72**	**1**	**3.9**

Table 6.1 Measurement errors.

It is known that Nb_3Sn is strain sensitive, and variations of the strand intrinsic strain could affect the results. But contrary to I_c measurements that are very sensitive to strain, this does not occur for magnetization, where the only currents flowing in the sample are local currents due to magnetization itself, and even if some filaments are broken there is no measurable difference.

Another parameter that has to be considered is temperature. There are no temperature sensors on the sample. To apply a Cernox on the strand is not an easy operation because the sensor has to be thermally isolated from the liquid helium and carefully soldered to the sample. The temperature sensor in the VTI is used to monitor the temperature during the measurement. Since there is no transport current flowing in the sample, the only heat source is the solenoidal magnet when its field is ramped. A small variation of about 10 mK is the typical temperature variation range, whose effect is negligible.

To check the validity of the computed error analysis, a calibration of the system was performed.

6.3 CALIBRATION

To obtain an absolute calibration of the system, the Meissner state of pure Nb alloys was used, *i.e.* the magnetic field range below the lower critical field, B_{c1}. In this state, the superconductor presents a reversible magnetization, and generates currents that perfectly shield the material from the external field. Therefore, recalling equation 2.1:

$$B = B_0 + \mu_0 M = 0 \qquad \Rightarrow \qquad \mu_0 M = -B_0. \tag{6.2}$$

In the Meissner phase, the magnetization curve in the (B_0, $\mu_0 M$) space must be a line with a slope of –1. This can also be seen from the measurement shown in Figure 6.1.

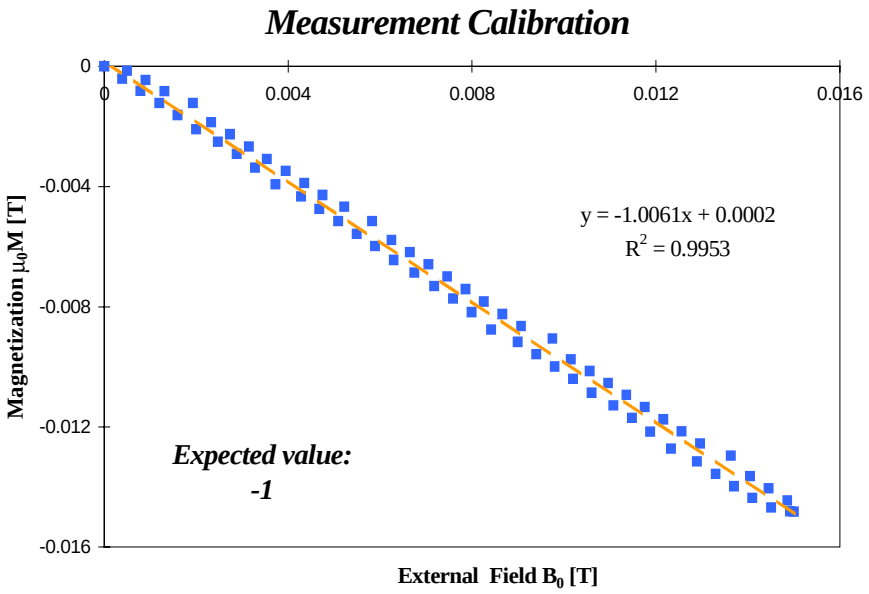

Figure 6.1 Calibration measurement using an RMC Niobium rod.

Niobium rods were used to check the calibration. This configuration was chosen for two reasons:

- simple geometry,
- measurement independence from the copper to non-copper ratio.

The simpler geometry is important to minimize the geometrical error, so that the error measured through calibration is representative of the error of the integrated signal, that is harder to compute. The cross section area of a niobium rod can be measured much more accurately than that of the coil used for a multifilamentary strand.

The second advantage is that with a rod of pure superconducting niobium, the effective copper to non-copper ratio needs not to be considered. This parameter cannot be known because after reaction, the non-copper fraction in the Nb_3Sn strand includes both the superconductor and the bronze between the filaments. The bronze can act as weak superconductor in the vicinity of the filaments, modifying the real superconductor content and magnetization. This phenomenon introduces an unacceptable uncertainty in the calculation of the slope during the Meissner state, invalidating the results.

The magnet was swept up to 15 mT at the low ramp rate of 20 mT/min to minimize eddy currents. The measured B_{c1} for niobium is 180 mT. The data shown in Table 6.2 confirm that the average error on the slope is very close to the integrated signal uncertainty.

Material	Slope
Ideal	-1.0000
Teledyne	-1.0138
Cabott	-1.0138
RMC	-1.0061
Average	**1.011**

Table 6.2 System calibration using niobium rods.

6.4 SUMMARY

The calibration of the system confirmed the reliability of the balancing coil magnetometer developed at the Short Sample Test Facility at Fermilab's Technical Division. Data can be compared with measurements done in other

laboratories with different setups. The investigation of the magnetic properties of multifilamentary superconducting Nb_3Sn and NbTi strands will be presented in the next section.

CHAPTER

7

RESULTS AND APPLICATIONS

7.1 INTRODUCTION

In this chapter, the magnetization measurements of superconducting multifilamentary NbTi and Nb_3Sn strands are presented. In a first instance, how the geometric-magnetic properties of composite superconductors, *i.e.* effective filament diameter, d_{eff}, can be inferred from the hysteresis curve is discussed. Magnetic properties of Nb_3Sn were investigated for existent manufacturing technologies. The critical fields of a number of Nb alloys were also measured. Finally, the usefulness of magnetization measurements is described when studying effects such as critical current degradation due to cabling, heat treatment impact on the wire performance, and alike.

7.2 MAGNETIC PROPERTIES

The basic result of the measurements performed with the setup described in Chapter 4 is the hysteresis curve of the material. The measurement cycles can be performed by sweeping the external magnetic field through the positive and

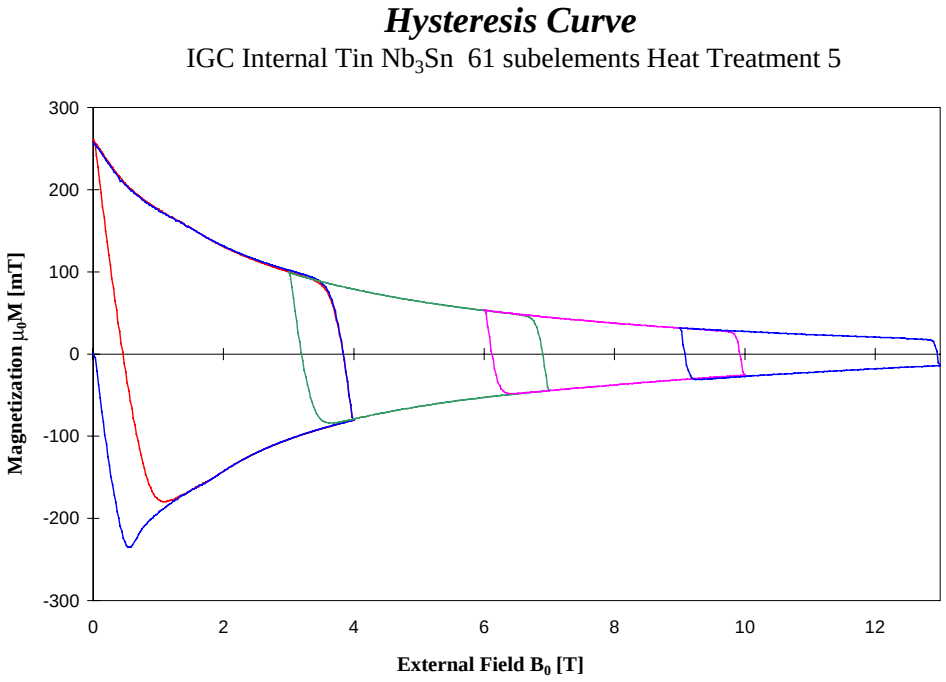

Figure 7.1 Monopolar hysteresis curve of a Nb_3Sn superconducting strand.

negative polarity. However, in a bipolar cycle around zero field some errors occur due to the change in polarity of the magnet. In order to avoid this phenomenon, and to minimize the variation of the integrator drift, monopolar cycles are usually performed in an external magnetic field range of only 0-3 T with a ramp rate of 1 T/min.

Figure 7.1 shows the monopolar hysteresis curve from zero to 13 T of an IGC Internal Tin 1 mm Nb_3Sn strand with 61 split-subelements. In this particular case, four loops, each of them covering a 4 T range, are superimposed. The ramp rate was raised to 1.5 T/min, since the effect of eddy currents is negligible. The result is a complete hysteresis curve over a wide range of external magnetic fields.

To characterize the material, usually two different loops are performed as shown in Figure 7.2 and 7.3. The first at low field, from 0 to 3 T, and the second at high field, from 6 to 9 T for NbTi and from 10 to 13 T for Nb_3Sn.

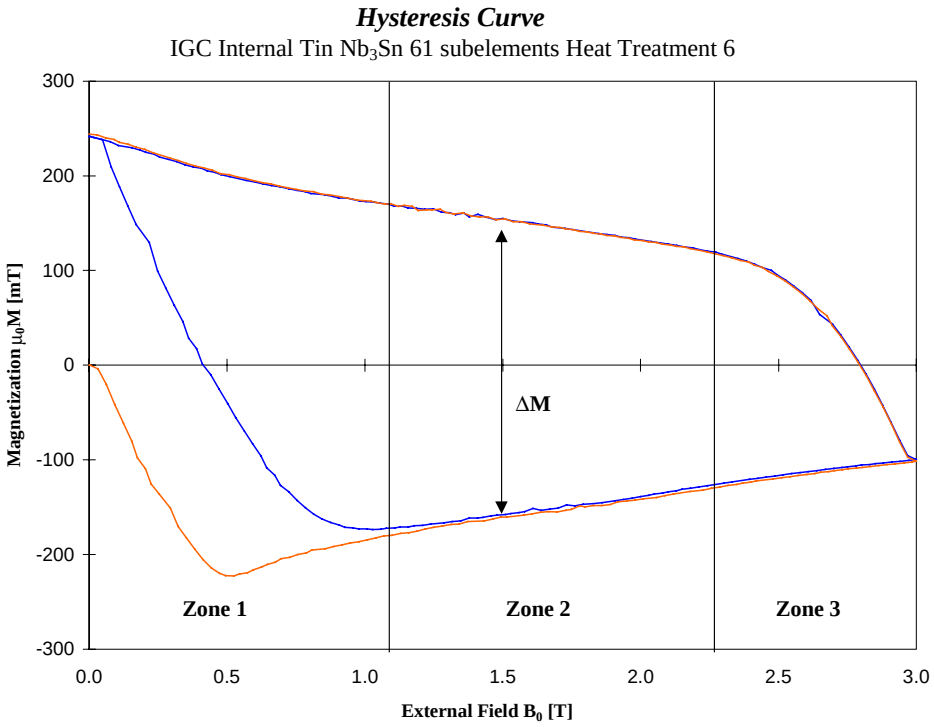

Figure 7.2 Low field loop for a Nb_3Sn strand.

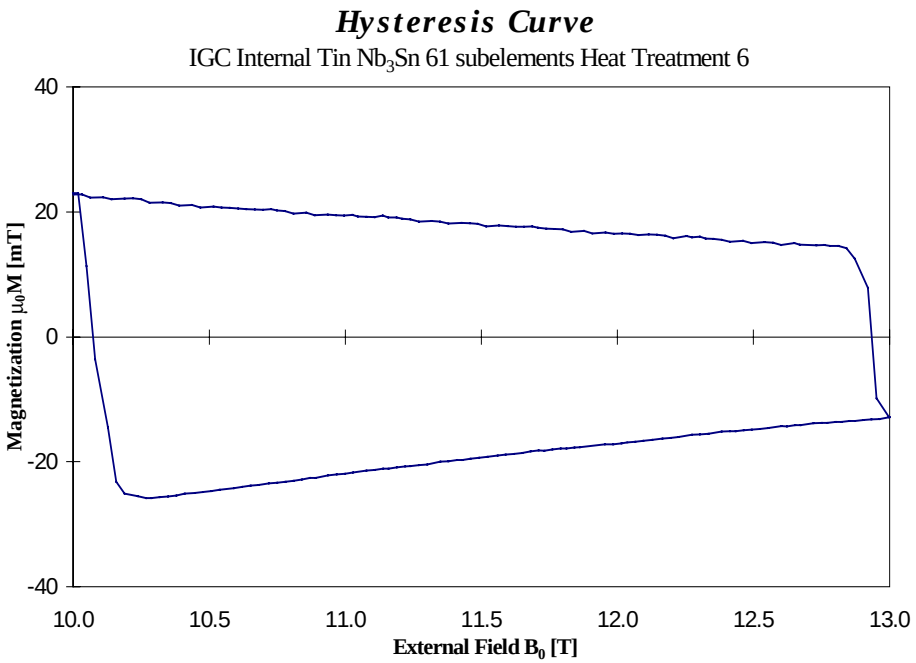

Figure 7.3 High field loop for a Nb_3Sn strand.

At the start (B=0) of the first magnetization cycle of a virgin magnetic state, M=0. When the loop is over, a residual magnetic flux is left in the material bulk, *i.e.* $M \neq 0$ at B=0. The resulting curve is not a closed cycle and is called *first magnetization curve*. However, any subsequent cycle will be a closed loop. This information can be used to correct for any drift generated by the integrator for magnetization cycles following the first. Since this property cannot be exploited for the first cycle, the correct representation of the first magnetization curve is not readily achievable. The drift for this measurement has to be deduced from the one found in the successive cycles and this introduces considerable error.

As shown in Figure 7.2 and in the scheme of Figure 2.9 the monopolar hysteresis loop can be divided in three different zones. The first one almost coincides, for the first magnetization curve, to the Meissner state, when the external field has not yet fully penetrated the bulk of the strand. In successive cycles, this zone is a transition region in which the field inside the material changes polarity. The second zone shows the material fully penetrated by the field. The third zone describes a change in direction of the external magnetic field that causes a gradual inversion in polarity of the magnetization currents inside the material. Due to the flux pinned in the superconductor, a residual magnetic field offsets the curve from the initial path generating the characteristic loop. Only the second zone, *i.e.* fully penetrated strand, is useful for the calculation of the strand magnetization.

Magnetization can be calculated either over the whole strand cross section or over the superconducting fraction only. The latter method is useful when comparing different designs or manufacturing methods. The first is preferred here to avoid introducing the copper to non-copper ratio in the calculations, thus minimizing errors in the results.

The area of the hysteresis loop represents the work done by the power supply of the magnet that provides the external magnetic field, and corresponds to the total energy loss in the sample due to its magnetization:

$$Q = \oint M dB_0 = -\oint B_0 dM , \tag{7.1}$$

The losses due to the hysteresis curve, and those related to the eddy currents are a major issue in magnet design, since they represent a considerable heat load for the cryogenic system. One of the objectives in conductor design is to reduce them as much as possible. To make a comparison among different strands, the area of the loop between 0 and 3 T was calculated.

There are several models for correlating the magnetization to persistent currents in the wire. In the critical state model, intoduced in section 2.5, the current density, *J*, in a filament can assume only two different values: zero or the critical density, J_c. Figure 7.4 recalls the model predictions for a filament in a varying external field.

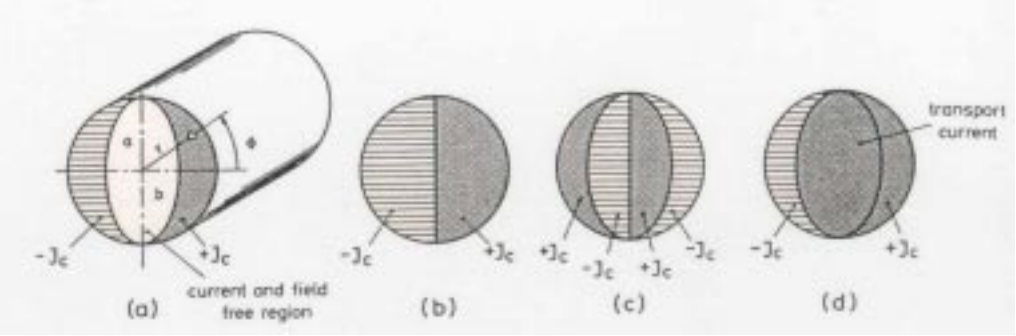

Figure 7.4 Schematic view of the persistent currents which are induced in a superconducting filament by a varying external field. (a) The external field is rised from zero to a value less then the penetrating field. (b) A fully penetrated filament. (c) Current distribution which results when the external field is first increased from zero to a certain value and then decreased again. (d) Same as (b) but with transport current.

The magnetization of the wire, by definition, is equal to the magnetic moment of the current per unit volume. Each filament of radius *r*, fully penetrated, has a magnetic moment per unit length, Γ, of [27]:

$$\Gamma = \int_{-r}^{r} 2J(\rho)\rho\sqrt{r^2 - \rho^2}\,d\rho, \tag{7.2}$$

Since *J* at constant temperature assumes only the critical value $J_c(B_0)$, the magnetic moment becomes:

$$\Gamma = \frac{1}{6} J_c d_{eff}{}^3, \tag{7.3}$$

where d_{eff} is the effective filament diameter ($2r$).

The magnetization calculated on the total strand cross section, A, of a multifilamentary strand with N filaments is:

$$M = N \frac{\Gamma}{A}, \tag{7.4}$$

which, together with equation 7.3, leads to:

$$M = \frac{1}{6} d_{eff}^3 N \frac{J_c}{A}. \tag{7.5}$$

Equation 7.5 was expressed in terms of measurable parameters, thus reducing propagation errors. The direct measurement on the wire gives I_c rather than J_c. One can make use of the following relation:

$$I_c = \pi N \frac{d_{eff}^2}{4} J_c, \tag{7.6}$$

in order to rewrite equation 7.5 as:

$$M = \frac{2}{3\pi} d_{eff} \frac{I_c}{A}. \tag{7.7}$$

This equation shows the correlation between magnetization, critical current, and effective filament diameter, which are the three parameters that characterize the multifilamentary strand. For any two known parameters, the third one can be calculated.

7.3 MATERIAL CHARACTERIZATION

Well known NbTi wires were used to verify the reliability of the measurements obtained. Nb_3Sn samples were tested to study strands produced by a number of companies with different manufacturing technologies. A majority of the measurements were performed on strand produced by IGC with the internal tin method. However, also composite wires produced with modified jelly roll and powder in tube methods were investigated.

7.3.1 NbTi strand

The necessity of reaching high field gradients for the interaction region quadrupole magnets of LHC [28] promoted an R&D program on a post-SSC NbTi strand with high iron content. Fermilab, together with IGC Advanced Superconductors, Oxford Instruments Superconducting Technology, (OST), and the Applied Superconductivity Center at University of Wisconsin in Madison, participated in this program.

The specifications for the NbTi previously developed for the SSC project limited the iron content in the strand to a maximum of 200 ppm Fe. For the LHC high gradient quadrupole magnets (HGQ), a strand showing a Fe content of 600 ppm was developed. This improved the I_c by about 7% without showing any relevant increase in hardness. This significant result was achieved because the higher iron content allowed a more homogeneous and fine distribution of the α-Ti precipitates during the multiple heat treatments, thus intensifying flux pinning in the superconductor.

In order to test the reliability of the experimental setup for the magnetization measurement, two different NbTi high Fe superconductors were tested. Table 7.1 shows the measured properties of an IGC strand extracted from billet number B7363 1-1-9, and of a OST strand extracted from billet number 4163-1A2 [29]. The d_{eff} at 7.5T was calculated from the 6 to 9 T hysteresis loop, shown in Figure 7.5 for both materials.

	OST 4123-1A2	IGC 7363 1-1-9
Strand diameter [mm]	**0.805**	**0.818**
Cu content	**43.1%**	**43.1%**
Twist pitch [mm]	**9**	**-**
RRR	**162**	**-**
I_c (7.5 T) @ 4.2 K [A]	**345**	**359**
J_c (7.5 T) @ 4.2 K [A/mm^2]	**1525.60**	**1589.56**
$\mu_0 M$ (7.5 T) @ 4.2 K [mT]	**1.77**	**1.25**
AC Losses 0-2 T @ 4.2 K [kJ/m^3]	**95.43**	**-**
Effective filament diameter d_{eff} [μm]	**10**	**7**

Table 7.1 NbTi strands properties and measured data.

The d_{eff} values of Table 7.1 show the usefulness of double layer samples for NbTi strands, which usually have a very low magnetization. The IGC sample was a single layer coil (see section 4.7), and the d_{eff} value derived from the magnetization measurement (7 μm) was significantly different from the real value (10 μm). The OST specimen was double layered in order to increase the signal to background ratio. The 10 μm d_{eff} obtained for the OST sample was consistent (within its measurement uncertainty) with the 9.5 μm provided by the company.

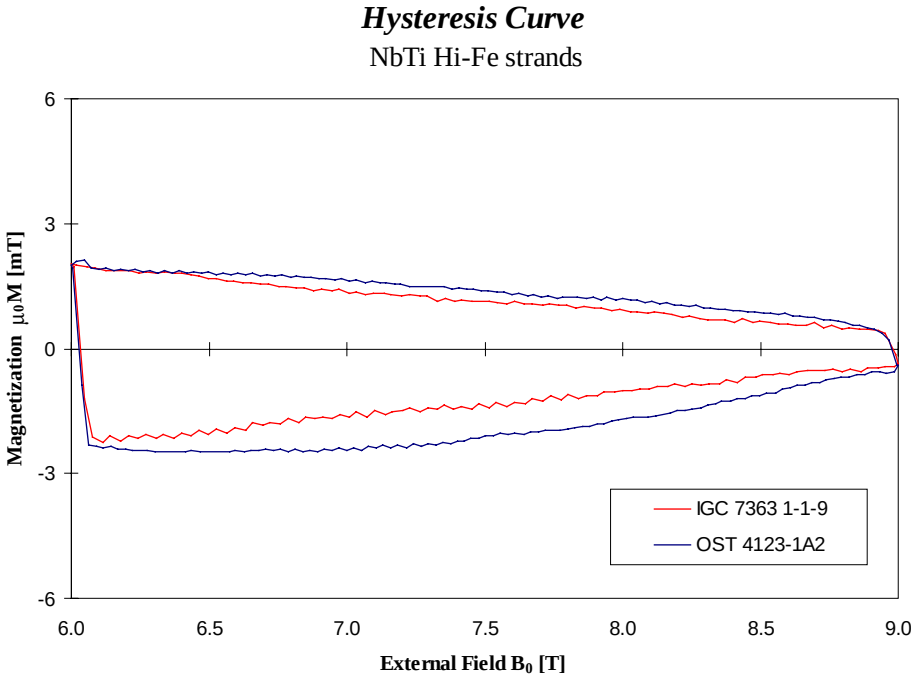

Figure 7.5 High field loops for NbTi strands.

This achievement allowed switching to Nb_3Sn with full confidence in a reliable setup.

7.3.2 Internal Tin Nb_3Sn

A majority of the samples tested within the short sample test facility were provided by IGC. Table 7.2 describes three of the investigated strands. Strand I was developed for the ITER-Euroatom project [30]. The main requirement of this conductor was a small d_{eff} to minimize field distortions and AC losses. The other two strands meant to reach I_c's high enough to be used in future high field magnets. All three strands were heat treated following the reaction schedule of Table 7.3.

	I	C	T
Strand diameter before reaction [mm]	1.000±0.001	0.999±0.001	1.000±0.001
Strand diameter after reaction [mm]	1.009±0.002	1.023±0.002	1.023±0.002
Split-subelements	19	37	61
Cu content	60%	46%	46%
Twist pitch [mm]	<10	15	15
Tin Content	Low	High	Intermediate
RRR	>100	>75	>75
I_c (12 T) @ 4.2 K [A]	230	639	533
J_c (12 T) @ 4.2 K [A/mm^2]	716	1507	1257
$\mu_0 M$ (12 T) @ 4.2 K [mT]	0.75	24.20	17.17
AC Losses 0-3 T @ 4.2 K [kJ/m^3]	69.91	802.8	553.9
Effective filament diameter d_{eff} [μm]	4.9	116	99

Table 7.2 IGC Internal tin Nb_3Sn strand properties and measured data.

Heat Treatment 5	Rate [K/hr]	Temperature [°C]	Hours
Step 1	**25**	**575**	**200**
Step 2	**25**	**700**	**90**

Table 7.3 Heat treatment schedule.

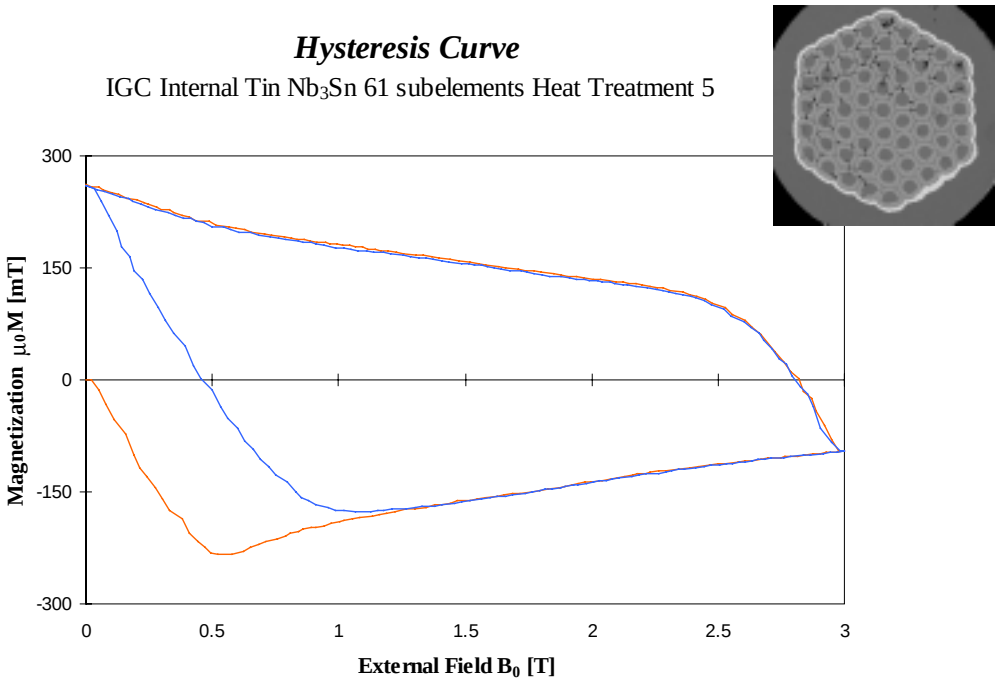

Figure 7.6 Low field loop for IGC Nb_3Sn 61 split-subelements.

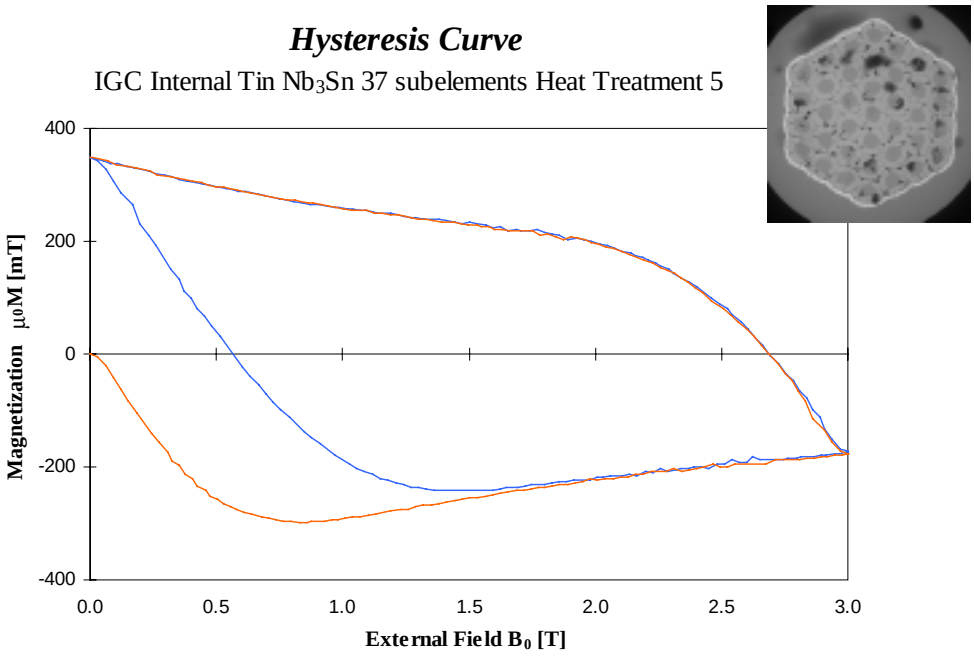

Figure 7.7 Low field loop for IGC Nb_3Sn with 37 split-subelements.

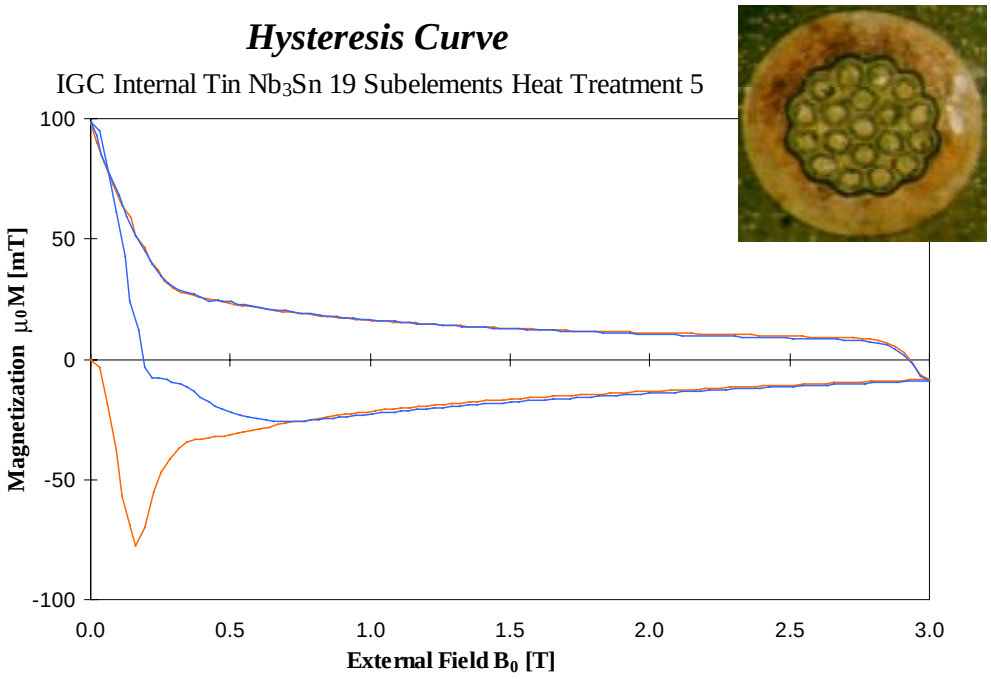

Figure 7.8 Low field loop for IGC Nb_3Sn with 19 split-subelements.

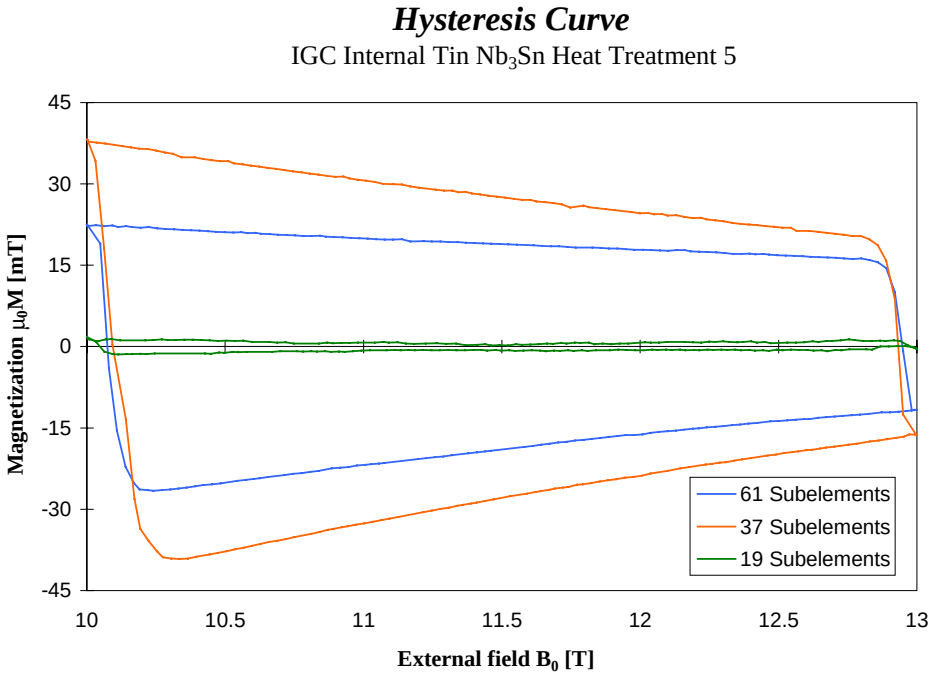

Figure 7.9 High field loops for internal tin Nb_3Sn.

Data show that strand C reaches the highest J_c. This result is probably due to the higher tin content, which allows the formation of more superconductor during the thermal reaction. However, because of the lower number of subelements of strand C with respect to strand T, the former has larger d_{eff} and higher AC losses (calculated on the total volume of strand). Strand I shows a very small d_{eff}, comparable to NbTi, but J_c is very small. The hysteresis curves at low and high fields of these materials are shown in Figure 7.6, 7.7, 7.8,and 7.9.

7.3.3 Modified Jelly Roll Nb_3Sn

At present, modified jelly roll Nb_3Sn is proably the superconductor showing the most advanced state of development. Some conductor produced with this technology has been measured in order to investigate its properties. Table 7.4 shows the characteristics of the material and some measured data, while in Figures 7.10 and 7.11 the loops at low and high field are presented. This strand achieved the highest J_c value ever measured at the SSTF. But since its effective filament diameter is comparable to that of the lower I_c strands (about 100 μm), the phenomenon of flux jumping was also detected, as predicted by the model described in section 3.2.

	Oxford MJR
Strand diameter before reaction [mm]	**0.798±0.001**
Strand diameter after reaction [mm]	**0.810±0.001**
Cu content	**53%**
Twist pitch [mm]	**-**
Tin Content	**-**
RRR	**-**
I_c 12 T @ 4.2 K [A]	**534**
J_c 12 T @ 4.2 K [A/mm^2]	**2200**
$\mu_0 M$ 12 T @ 4.2 K [mT]	**30**
AC Losses 0-3 T @ 4.2 K [kJ/m^3]	**820**
Effective filament diameter d_{eff} [μm]	**108**

Table 7.4 Modified jelly roll Nb_3Sn properties and measured data.

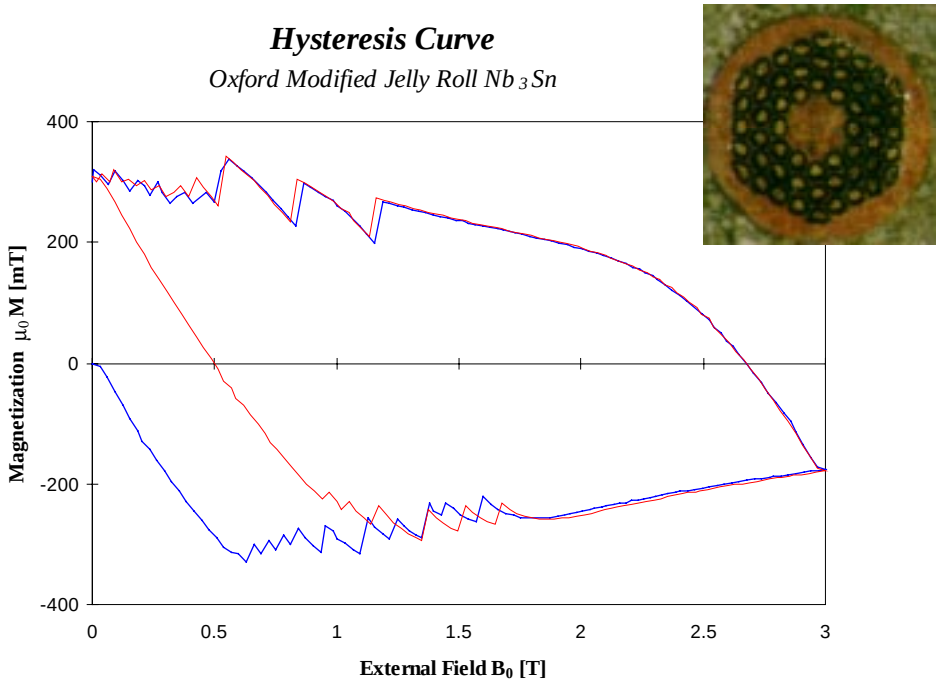

Figure 7.10 Low field loop for Oxford MJR Nb_3Sn.

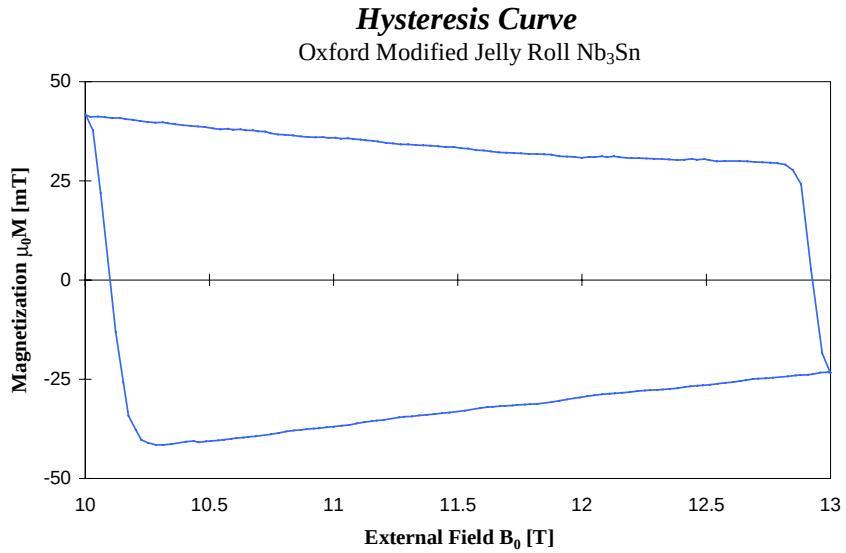

Figure 7.11 High field loop for Oxford MJR Nb_3Sn.

7.3.4 Powder in Tube Nb_3Sn

The main feature of the strand produced with this technology is the short thermal reaction time necessary to obtain the superconducting compound. A strand with 36 subelements was measured after a heat treatment of only 100 hours. The thermal reaction schedule is shown in Table 7.5, while the strand properties and measured data are presented in Table 7.6. The d_{eff} could not be calculated due to I_c data missing (the samples showed a resistive behavior that invalidated I_c tests, either due to mechanical strain during preparation or to a large current transfer length). Figure 7.12 shows some instability in the low field loop. This phenomenon is probably due to the large filament size, since this strand had only 36 filaments.

PIT Strand type	Rate [K/hr]	Temperature [°C]	Hours
36 subelements	**25**	**675**	**100**

Table 7.5 Heat treatment schedule.

	PIT
Strand diameter before reaction [mm]	0.898±0.001
Strand diameter after reaction [mm]	0.913±0.001
Subelements	36
Cu content	45%
Twist pitch [mm]	25
Heat Treatment [hr]	100
RRR	-
I_c 12 T @ 4.2 K [A]	-
J_c 12 T @ 4.2 K [A/mm^2]	-
$\mu_0 M$ 12 T @ 4.2 K [mT]	26.12
AC Losses 0-3 T @ 4.2 K [kJ/m^3]	660.10
Effective filament diameter d_{eff} [μm]	-

Table 7.6 Powder in tube Nb_3Sn strand properties and measured data.

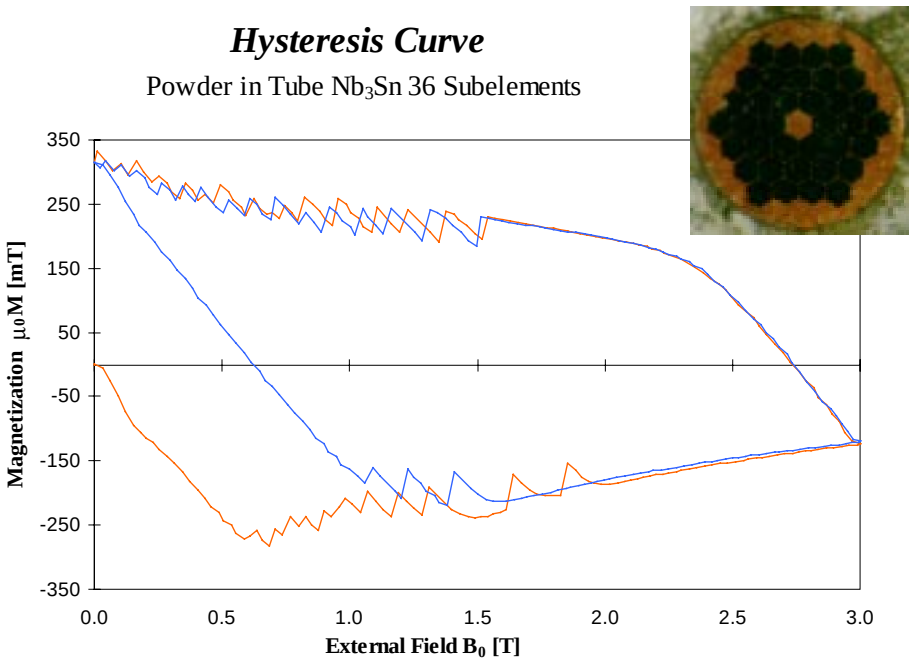

Figure 7.12 Low field loop for PIT Nb_3Sn.

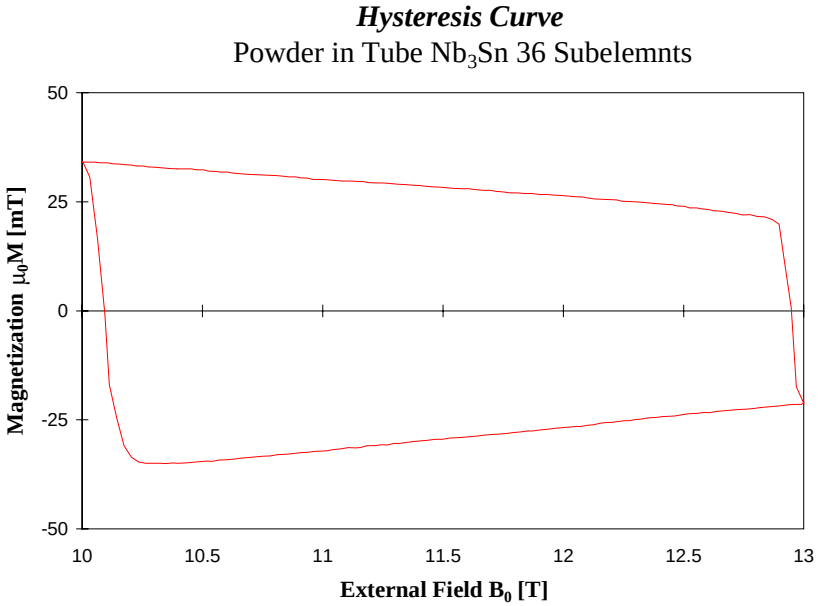

Figure 7.13 High field loop for PIT Nb_3Sn.

7.4 NIOBIUM AND CRITICAL FIELDS

The quality of Nb is well known to be an important parameter in the manufacture of superconducting RF cavities. Its purity is often referred to as RRR (residual resistivity ratio). However, above 200, the RRR is not a measure of Nb purity anymore.

A different way of observing lattice imperfections in Nb is by the fluxoid motion in the superconductor, represented by its magnetization [31, 32]. Various rods of Nb alloys were tested to understand if Nb quality affects the performance of Nb_3Sn strands. Nb is interesting also because it lies on the border between type I and II superconductors, with a relatively high B_{c1} and a low B_{c2}. Its characteristics allowed to measure these two fields and to calibrate the system (see Section 6.3). The data obtained were sent to the company that produces Nb_3Sn as a new tool to improve their material.

Six cylindrically shaped samples from three different companies were tested. The diameter varied within the 11 to 14 mm range. These rods were

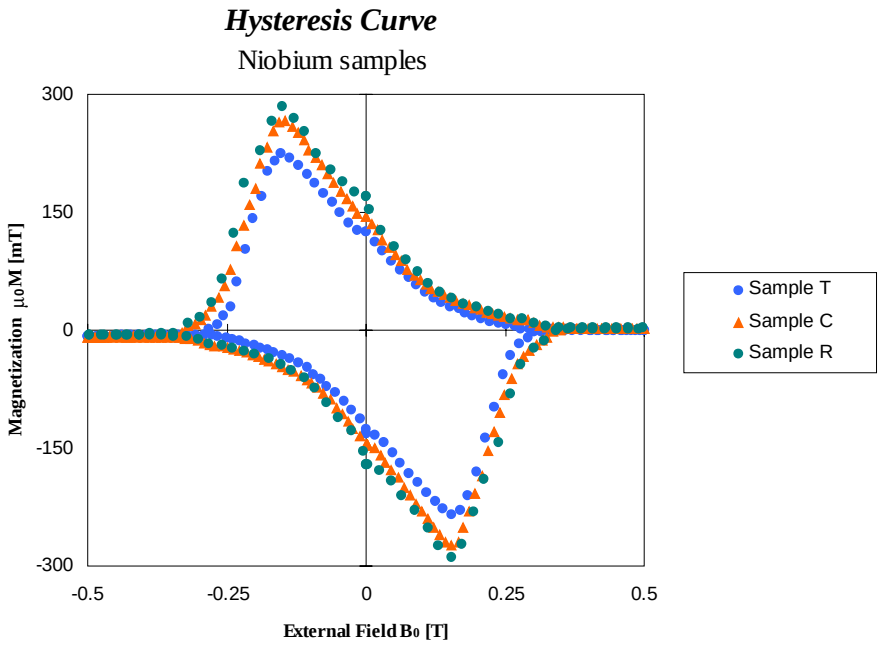

Figure 7.14 Bipolar hysteresis loops of Nb alloys.

manually cut to a length of 100 mm using a saw. Figure 7.14 shows the measured hysteresis curve of three of the Nb samples, while the results on critical fields are presented in Table 7.7. The small distortion of the hysteresis curves around $B_0 = 0$ is due to the change in polarity of the magnet.

	T	C	R
Length [mm]	100.44	100.51	102.40
Cross section [mm^2]	108.45	171.01	170.86
B_{c1} [mT]	181	180	180
B_{c2} [mT]	316	340	330
Magnetization @ B_{c1} [mT]	-162	-154	-160

Table 7.7 Nb alloys properties and measured data.

A fourth Nb sample showed significant flux jumping, as can be seen in Figure 7.15. This was the only case of flux jump observed and it could be explained by the high tantalum content in the alloy.

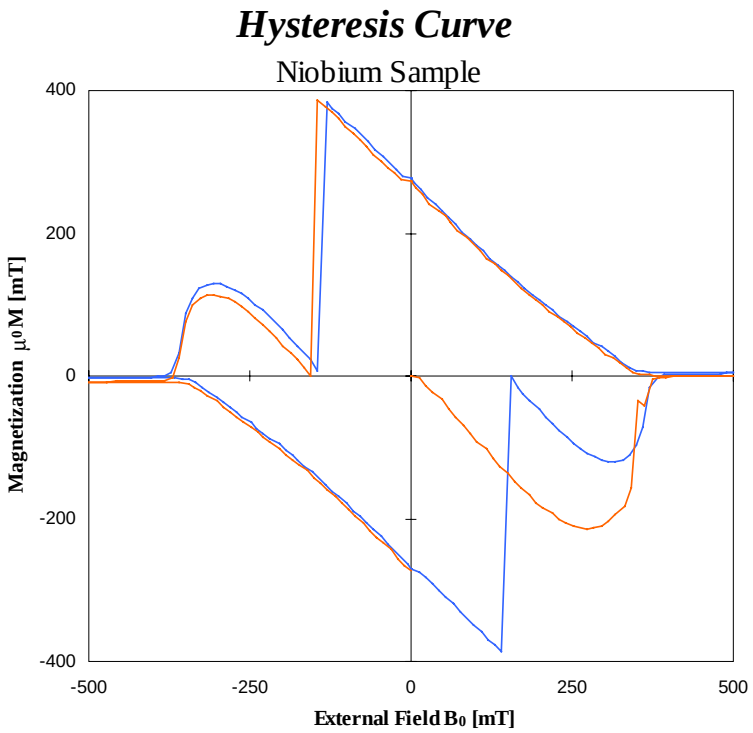

Figure 7.15 Bipolar hysteresis loop of Nb rod showing flux jump.

7.5 CABLING DEGRADATION

The critical current, I_c, of the original virgin strand is reduced during magnet fabrication. Among the factors that reduce I_c are strand deformation during cabling, which occurs before reaction, and cable compression in the coil, which is applied after the magnet coils have been reacted. This latter factor is due to I_c sensitivity of Nb_3Sn to strain. In this Section, results of I_c degradation due to cabling are presented [33].

Rutherford cable samples with different packing factors were fabricated at LBNL, and extracted strands were tested at Fermilab (see Figure 3.3). The packing factor, P, of a cable is defined as the ratio of the cross section occupied by the strands to the overall cross section of the cable:

$$P = \frac{\pi n d^2}{2w(t_1 + t_2)\cos\psi}, \tag{7.8}$$

where t_1 and t_2 are the minor and the major edge thickness. The other properties of the cable are defined in Table 7.8. Different packing factors were obtained by varying the average cable thickness, which was 1.816 mm, 1.797 mm, 1.785 mm, 1.758 mm, corresponding to packing factors of 90%, 91%, 91.6%, and 93% respectively.

	value
Strand diameter, d [mm]	**1.012±0.001**
Number of strands, n	**28**
Cable width, w [mm]	**14**
Keystone angle, Φ	**1.021**
Lay angle, Ψ	**14.53**

Table 7.8 Cable parameters.

The I_c degradation as a function of the magnetic field and of the cable packing factor for a strand reacted with a nominal heat treatment is shown in Figure 7.16. It can be seen that the I_c degradation depends on B, with an indication of an increasing effect with higher packing factor and higher field.

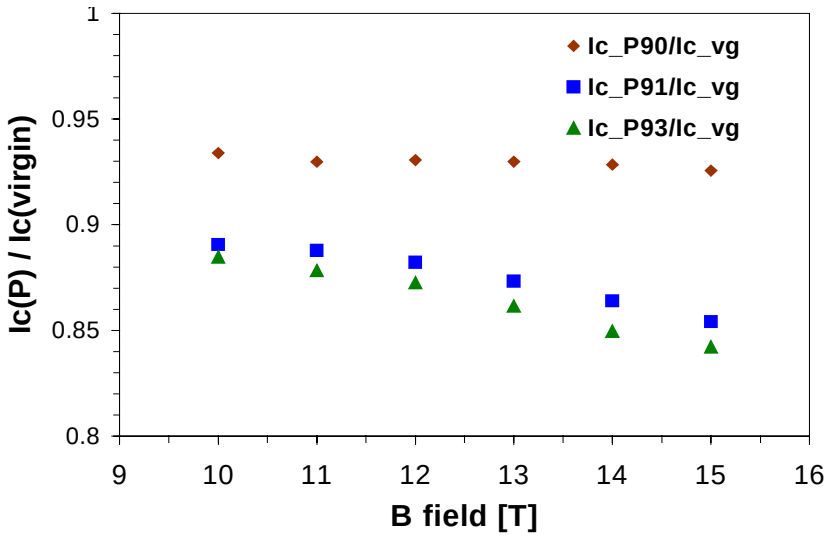

Figure 7.16 Normalized I_c as a function of magnetic field for extracted strands.

The results of this study show that the I_c degradation due to cabling is relatively low for the cables made of internal tin Nb_3Sn strand. For the cable with the largest packing factor (93%), it is less than 13% at 12 T and less than 16% at 15 T, and it can be kept lower than 7% by choosing a cable with a packing factor below 90%. In order to understand the possible causes of this degradation, additional studies were performed. Figure 7.17 shows the magnetization between zero and 3 T of a virgin strand and of a strand extracted from the cable with the maximum packing factor. The width of the magnetization loop being proportional to the local J_c in the superconductor, the hysteresis loops show that there is no observable J_c degradation at low fields. The AC losses were 436.9 kJ/m^3 for the virgin strand, and 438 kJ/m^3 for the extracted strand, *i.e.* practically the same. On the contrary, as can be seen in Figure 7.18, the AC losses at high fields of the virgin strand and of the extracted strand differ by 9%. This is consistent with I_c degradation increasing with field, as shown in Figure 7.16.

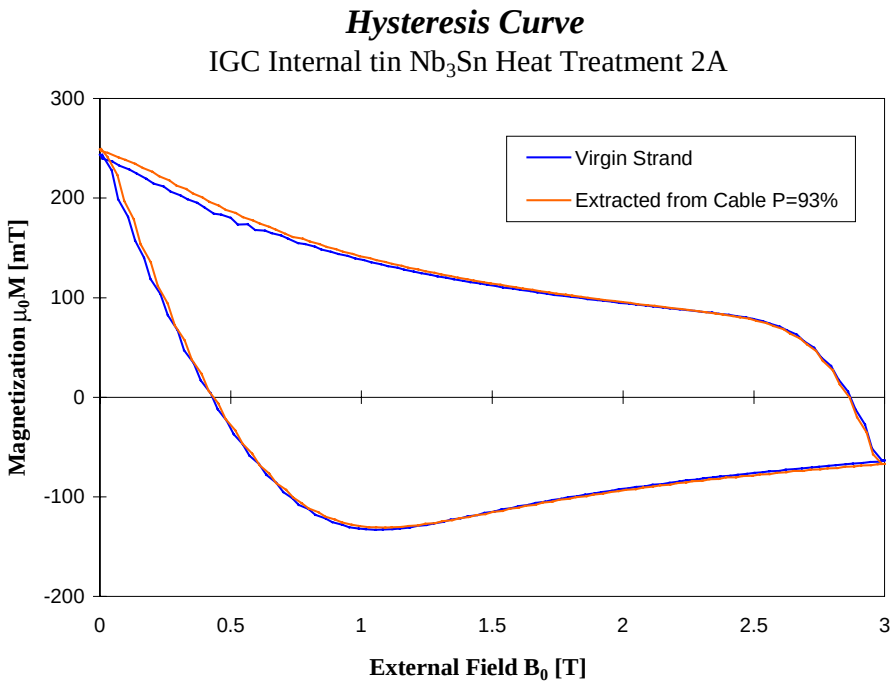

Figure 7.17 Magnetization loops at low field for the virgin and the extracted strand with P=93%.

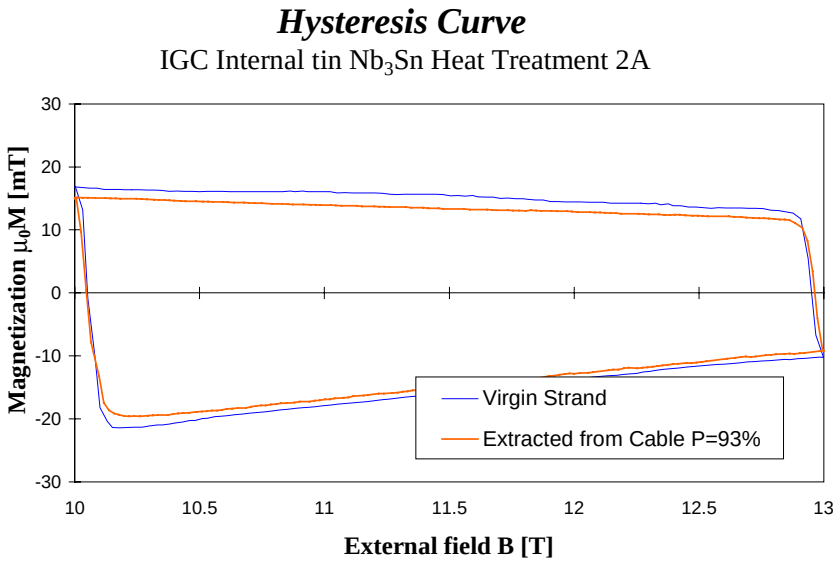

Figure 7.18 Magnetization loops at high field for the virgin and the extracted strand with P=93%.

The following additional parameters were also investigated:

- n-values, which is a quality factor related to the longitudinal uniformity of the superconducting filaments;
- damage of the diffusion barrier and tin leakage into the outer copper, by measuring the copper residual resistivity ratio (RRR);
- non uniformity of tin diffusion in the deformed part of the strand cross section, by performing a point to point compositional analysis of the Cu-Sn matrix and of the Nb-Sn filaments by energy dispersion X-rays (EDX);
- strand cross section reduction at cable edges, by measuring the cross sectional areas of virgin and extracted strands on their SEM pictures.

All these parameters, but the last one, show no significant variation due to cabling. From the SEM pictures, some significant area reduction of the non-copper part was measured for the extracted strands. This also contributes to a decrease of I_c.

The main mechanism in I_c cabling degradation appears to be area reduction at low fields and J_c degradation at high fields.

7.6 HEAT TREATMENT STUDY

The maximum field in a superconducting magnet is determined by the coil width and by the critical current density, J_c, of the superconductor. On the other hand, the field uniformity in the bore is very sensitive to superconductor magnetization, which is proportional to the effective filament diameter, d_{eff}, of multifilamentary strand, as seen in Section 7.2. Hence, for a cost effective and reliable magnet design, J_c should be as high, and d_{eff} as low as possible [34]. Strand R&D is actively pursued together with IGC using the internal tin process. A number of heat treatments were performed to understand their effect on the strand performance, and to try to optimize temperature and duration of the reaction. Three heat treatment cycles, differing in the temperature of their last

step, were applied to two Nb_3Sn strands, T and C, produced by IGC and whose properties are shown in Table 7.2.

The heat treatments were performed in an argon atmosphere using tube furnaces with the appropriate temperature uniformity over a length of 15 inches. The time schedule is given in Table 7.9 for HT-1, HT-2, and HT-3.

The AC losses for a 0 to 3 T loop at 1 T/min. and the d_{eff} at 12 T are shown in Figures 7.19 and 7.20 for both strands C and T as a function of the heat treatment. It can be seen that the d_{eff} increases with temperature while the behavior of the AC losses is slightly different for the two strands. The variation of the AC losses is small, while for the d_{eff} there is a significant improvement at the lower temperature.

	Heat treatment	Step 1	Step 2
Ramp rate, ^{o}C/h	**HT-1**	25	25
Temperature, ^{o}C		575	**650**
Duration, h		200	180
Ramp rate, ^{o}C/h	**HT-2**	25	25
Temperature, ^{o}C		575	**700**
Duration, h		200	90
Ramp rate, ^{o}C/h	**HT-3**	25	25
Temperature, ^{o}C		575	**750**
Duration, h		200	17

Table 7.9 Heat treatment cycles.

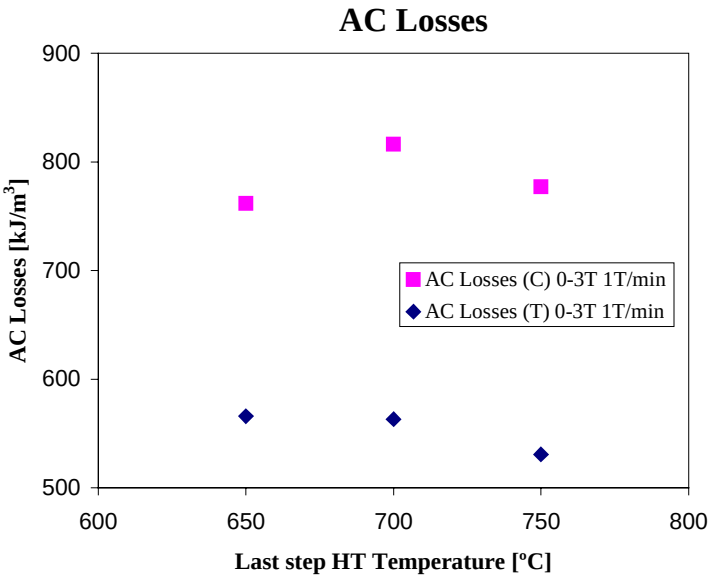

Figure 7.19 AC losses dependence on thermal cycle.

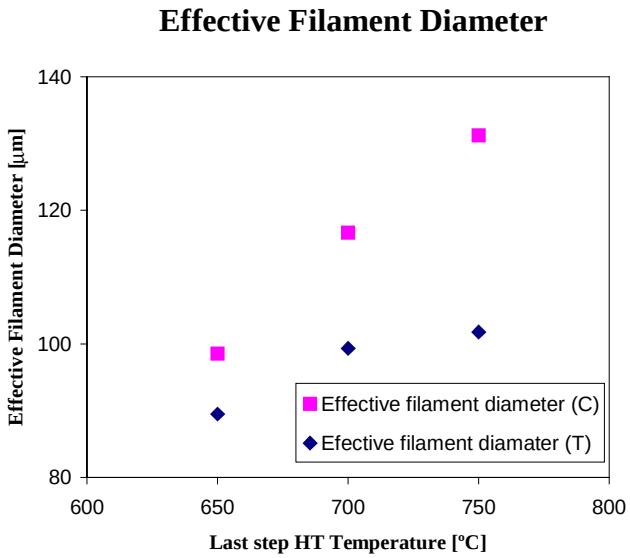

Figure 7.20 Effective filament diameter dependence on thermal cycle.

7.7 MAGNETIZATION AS A MEASURE OF CRITICAL CURRENT

The relation between M, I_c and d_{eff} is shown in equation 7.7. Its most common use is the calculation of d_{eff} by knowing I_c and M. For NbTi, the d_{eff} is the real filament diameter because superconducting filaments are well separated and independent entities. However, in Nb_3Sn the bronze induces proximity coupling (*i.e.* quantum-mechanical tunneling of Cooper pairs through the normal material between adjacent filaments), so that d_{eff} is usually much larger than the physical filament diameter. Such a weak superconducting behavior does not exclude that d_{eff} could be a function of the external magnetic field.

In order to investigate this effect, the hysteresis curve of a 1 mm IGC Nb_3Sn strand with 61 split-subelements was measured on a wide range of external fields from zero to 13 T (see Figure 7.1). The measurement of M and I_c at 12 T allowed to calculate the d_{eff} at this field. Data are shown in Table 7.10.

	value
Strand diameter after reaction [mm]	**1.023±0.001**
Ic @ 4.2 K 12 T [A]	**533**
μ_0M (12 T) @ 4.2 K [mT]	**38.53**
Effective filament diameter @ 12 T [μm]	**111.42**

Table 7.10 Effective filament diameter of Nb_3Sn strand at 12 T.

The critical current can be measured over a limited field range. The following relation, derived from Summers parametrization, was used to fit the measured I_c of a 0.8 mm Nb_3Sn strand with an equivalent design as that used for magnetization measurements:

$$J_c(B,T,\varepsilon) = \frac{C(\varepsilon)}{\sqrt{B}}\left[1-\frac{B}{B_{c2}(T,\varepsilon)}\right]^2\left[1-\left(\frac{T}{T_{c0}(\varepsilon)}\right)^2\right]^2,$$

$$\frac{B_{c2}(T,\varepsilon)}{B_{c20}(\varepsilon)} = \left[1-\left(\frac{T}{T_{c0}(\varepsilon)}\right)^2\right], \qquad (7.9)$$

$$B_{c20}(\varepsilon) = B_{c20m}(1 - a|\varepsilon|^{1.7}),$$

$$T_{c0}(\varepsilon) = T_{c0m}(1 - a|\varepsilon|^{1.7})^{\frac{1}{3}},$$

$$C(\varepsilon) = C_0(1 - a|\varepsilon|^{1.7})^{\frac{1}{2}},$$

where:

J_c	is the critical current density,
ε	is the strain,
B	is the magnetic field,
B_{c2}	is the upper critical field,
B_{c20}	is the upper critical field at zero temperature,
B_{c20m}	is the upper critical field at zero temperature and zero strain,
T_{c0}	is the critical temperature at zero field,
T_{c0m}	is the critical temperature at zero field and zero strain, and
a, C_0	are constants.

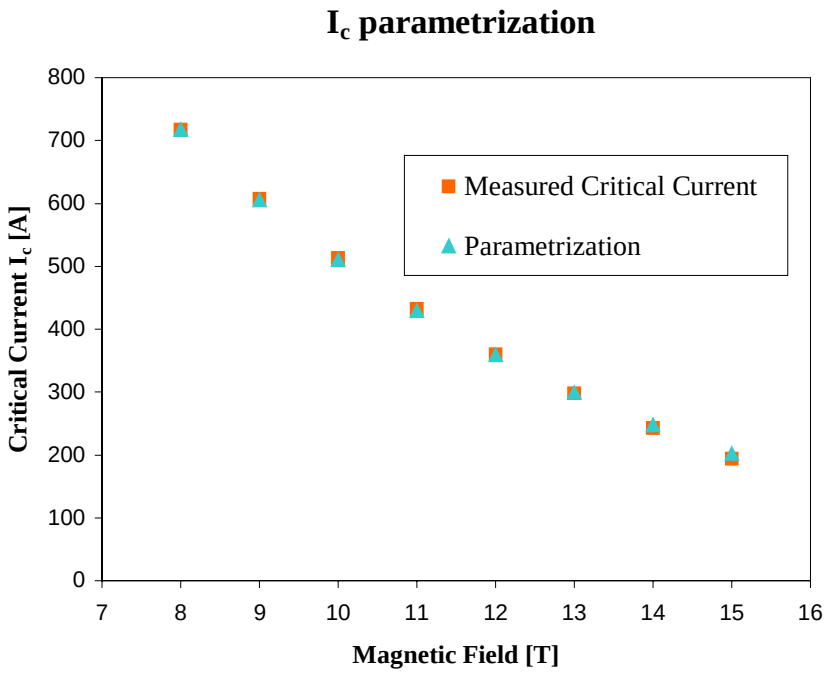

Figure 7.21 Critical current parametrization.

Figure 7.21 shows the comparison between the measured I_c and the values obtained with the above parametrization with B_{c20} = 28 T and T_{c0} = 18 K, and in the assumption of $\varepsilon = 0$.

Keeping the d_{eff} constant and equal to its measured value at 12 T, the I_c was calculated down to very low fields using the measured magnetization values.

These results were compared with the I_c's predicted by Summers parametrization. As can be seen from Figure 7.22, there is no significant difference down to 2 T, confirming that also for Nb_3Sn the d_{eff} does not depend on field (at least for fields down to 2 T), and therefore is a geometrical entity.

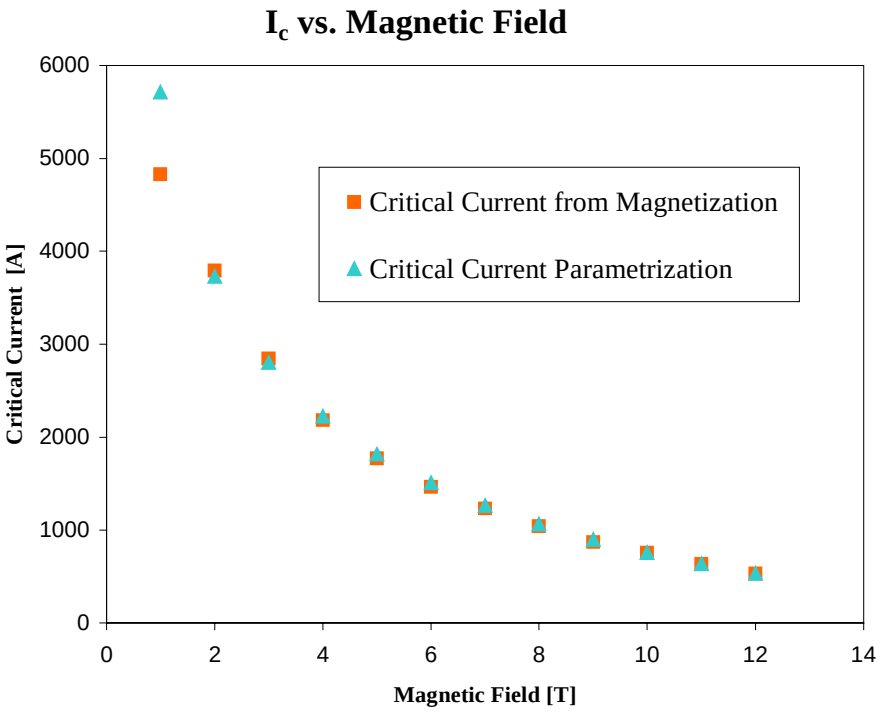

Figure 7.22 Critical current at low field from magnetization measurements and parametrization.

The parametrization can be also used in equation 7.7 together with the d_{eff} calculated at 12 T to obtain M as an analytical function of the external field. The comparison between the measured data and the parametrization is shown in

Figure 7.23. The representation of magnetization by an analytical function instead of single points is a significant achievement and a powerful tool for magnet design.

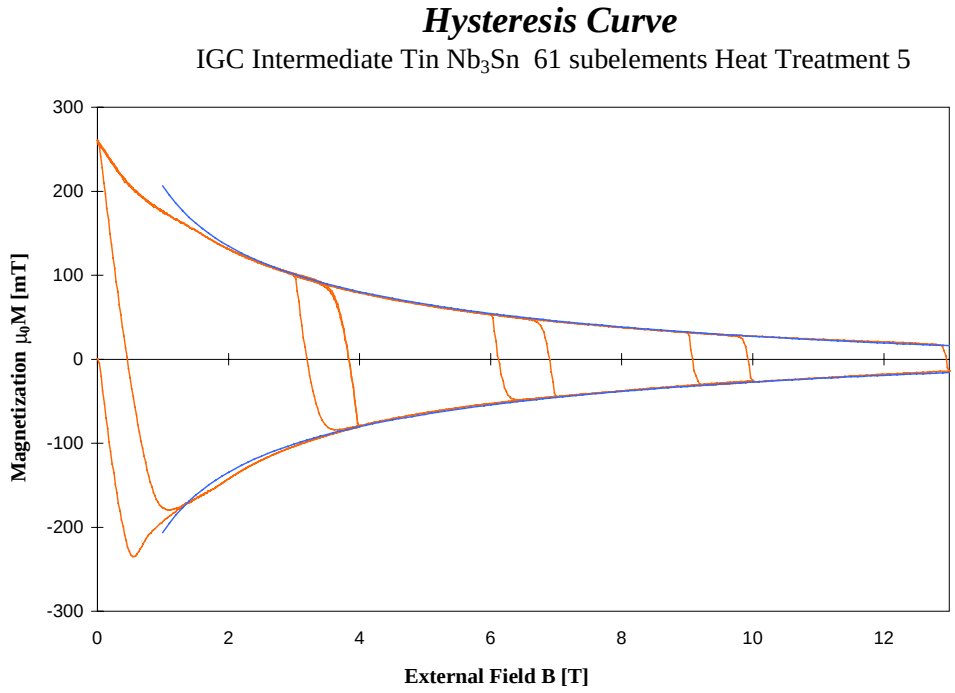

Figure 7.23 Parametrization of the hysteresis curve.

7.8 HOMOGENEITY STUDY OF A Nb_3Sn STRAND

Six spools of internal tin Nb_3Sn strand produced from the same billet were used to study the homogeneity of the strand properties along its length. The samples were reacted with heat treatment schedule HT-2, described in Table 7.9. Critical current and magnetization were measured at 12 T to obtain d_{eff}, as shown in Table 7.11.

Spool	I_c [A]	$\mu_0 M$ [mT]	d_{eff} [μm]
IT 2	558	18.39	101
IT 4-1	525	18.36	107
IT 4-2	533	17.19	99
IT 5	547	20.80	116
IT 6	521	21.69	128
IT 7	548	21.85	123
Average	539	19.5	112.5
Standard deviation	13	2	11.8

Table 7.11 Properties distribution at 12 T.

The measurement distribution for I_c and $\mu_0 \Delta M$, representing the distance between the two ramping branches of the hysteresis curve, are illustrated in Figures 7.24 and 7.25.

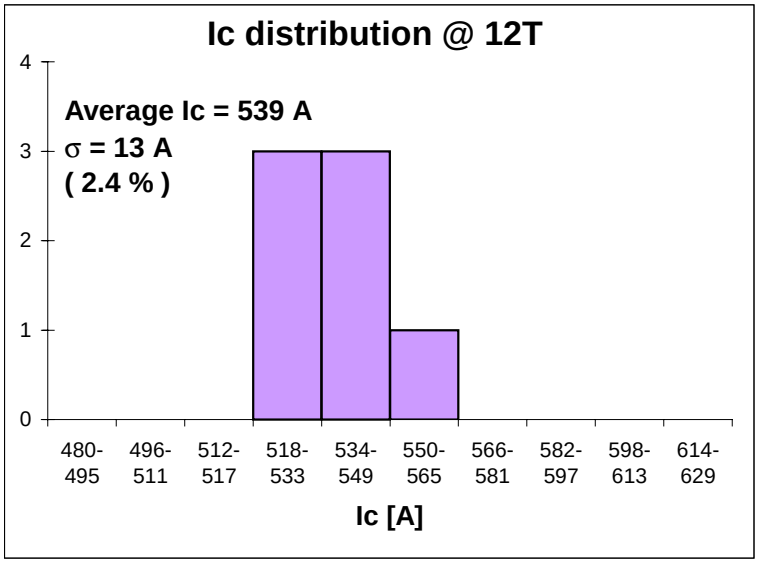

Figure 7.24 Critical current distribution.

Since the spread of the I_c measurements is very small (2.4%) and that of the magnetization measurements is comparable with the spread of d_{eff} (10% and 10.5% respectively), the inhomogeneity along the strand must be mainly related to geometrical variations.

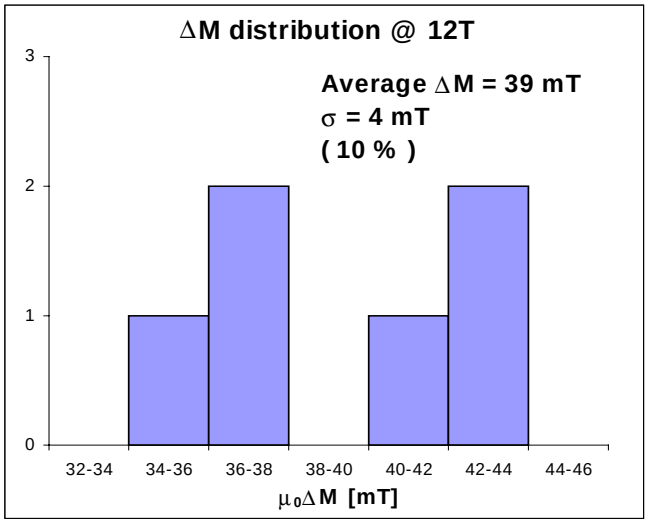

Figure 7.25 Magnetization distribution.

CONCLUSIONS

The initial goal of this thesis was to build the magnetometer and to perform initial tests to assess the reliability of the measurements. The realization of the magnetometer included designing the probe to position the sample in the magneto-cryostat, testing the electronics, and writing the data acquisition and analysis software. After completion of the setup, the device was tested. An accurate analysis of the parameters that influence the output signal was performed, and a calibration using niobium rod samples showed the reliability of the system.

This first phase lasted four months. In a second phase, a strong effort was devoted in characterizing the superconductor and in collecting useful data for magnet design and production.

The effect of the heat treatment on the internal tin Nb_3Sn strand has been the longest study, due to the long thermal reaction duration. However, data on strand produced with other technologies, like Modified Jelly Roll and Powder in Tube, were also collected. Magnetization measurements helped in understanding the mechanism of critical current degradation due to cabling by confirming the origin of the phenomenon. Finally, the independence of the effective filament diameter on magnetic field in Internal Tin Nb_3Sn strands was proved for fields down to 2T, and the homogeneity of the magnetic properties in different spools of the same billet was studied.

APPENDIX A

MAGNETO-CRYOSTAT SPECIFICATIONS

- **Superconducting vertical field solenoid magnet:**

Central field: 15 T @ 4.2 K/ 17 T @ 2.2 K

Clear bore: 64 mm diameter

Field homogeneity: 0.1 % over a 10 mm diameter spherical volume

Field stability in persistent mode: 1 part in 10^4/hr

Maximum magnet ramping speed: 1.6 T/min.

Resistor/diode protection 10 V

Switch mode power supply (120 A / +10 to -10V), bipolar

- **Dewar:**

Vapor shielded dewar, usable helium volume: 42 litres

Dewar fitted with helium level detector

Automated Lambda Refrigerator for 2.2 K operation

- **Variable Temperature Insert (VTI):**

Temperature range: 1.5 ÷ 200 K

Sample space: 49 mm

Heat exchanger fitted with Cernox sensor and heater

Automated needle valve control

- **Electronics**

Magnet power supply controller, GPIB interface

Temperature controller, 3 channels, GPIB interface

Helium double level meter, GPIB interface

Nanovoltmeter, 1nV sensitivity, GPIB interface

Electronics include LabView virtual instruments and drivers